

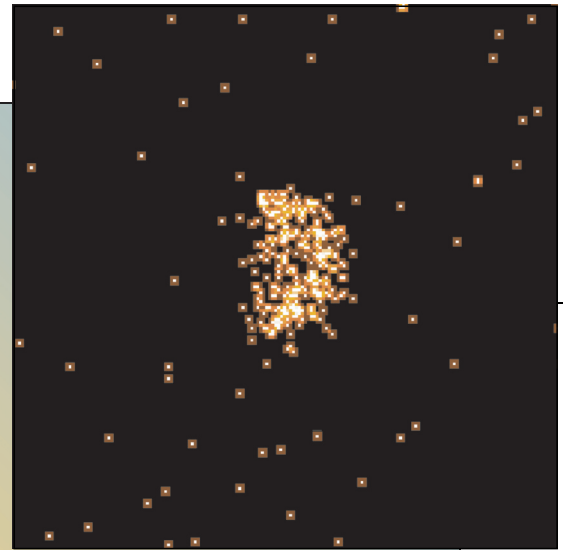
X-Rays in the Solar System

Anil Bhardwaj

Space Physics Laboratory
Vikram Sarabhai Space Centre
Trivandrum, India

Carey M. Lisse

Applied Physics Laboratory
Johns Hopkins University
Laurel, Maryland



CHAPTER 35

1. Introduction
2. Earth
3. The Moon
4. Venus
5. Mars

6. Jupiter
7. Galilean Satellites
8. Io Plasma Torus
9. Saturn
10. Rings of Saturn

11. Comets
12. Asteroids
13. Heliosphere
14. Summary

1. Introduction

The usually defined range of X-ray photons spans ~ 0.1 – 100 keV. Photons in the lower (< 5 keV) end of this energy range are termed soft X-rays. In space, X-ray emission is generally associated with high temperature phenomena, such as hot plasmas of 1 million to 100 million K and above in stellar coronae, accretion disks, and supernova shocks. However, in the solar system, X-rays have been observed from bodies that are much colder, $T < 1000$ K. This makes the field of planetary X-rays a very interesting discipline, where X-rays are produced from a wide variety of objects under a broad range of conditions.

The first planetary X-rays detected were terrestrial X-rays, discovered in the 1950s. The first attempt to detect X-rays from the moon in 1962 failed, but it discovered the first extrasolar source, Scorpius X-1, which resulted in the birth of the field of X-ray astronomy. In the early 1970s, the *Apollo 15* and *16* missions studied fluorescently scattered X-rays from the Moon. Launch of the first X-ray satellite UHURU in 1970 marked the beginning of satellite-based X-ray astronomy. The subsequently launched X-ray observatory *Einstein* discovered, after a long search, X-rays from Jupiter in 1979. Before 1990, the three objects known to emit X-rays were Earth, Moon, and Jupiter. In 1996, *Rontgensatellit (ROSAT)* made an important contribution

to the field of planetary X-rays by discovering X-ray emissions from comets. This discovery revolutionized the field of solar system X-rays and highlighted the importance of solar wind charge exchange (SWCX) mechanism in the production of X-rays in the solar system, which will be discussed in this chapter in various sections.

Today the field of solar system X-rays is very dynamic and in the forefront of new research. During the last few years, our knowledge about the X-ray emission from bodies within the solar system has significantly improved. The advent of higher resolution X-ray spectroscopy with the *Chandra* and *XMM-Newton* X-ray observatories (and now the next generation *SWIFT* and *Suzaku* observatories that are coming on-line in 2005–2006) has been of great benefit in advancing the field of planetary X-ray astronomy. Several new solar system objects are now known to shine in the X-ray (Fig. 1). At Jupiter, Saturn, Venus, Mars, and Earth, nonauroral disk X-ray emissions have been observed. The first soft X-ray observation of Earth's aurora by *Chandra* shows that it is highly variable, and the Jovian aurora is a fascinating puzzle that is just beginning to yield its secrets. The nonauroral X-ray emissions from Jupiter, Saturn, and Earth, and those from disks of Mars, Venus, and the Moon are mainly produced by scattering of solar X-rays. The X-ray emission from comets, the heliosphere, the geocorona, and the Martian halo are all largely driven by charge exchange between highly charged

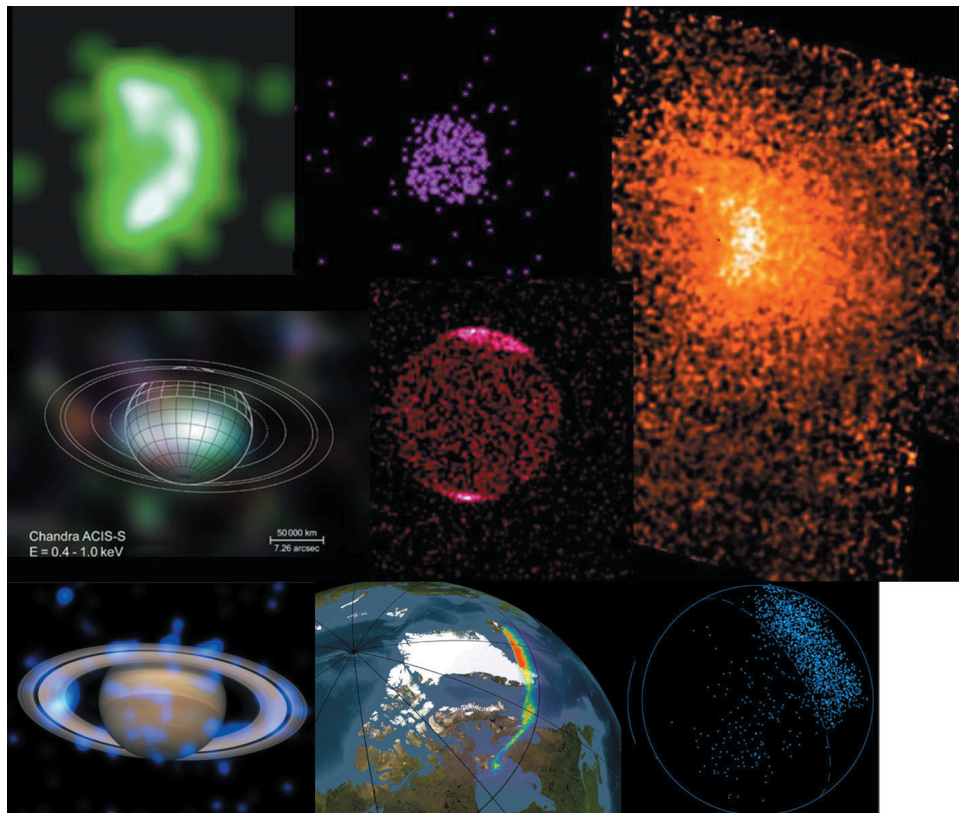


FIGURE 1 *Chandra* montage of solar system X-ray sources. Clockwise, from upper left: *Chandra* images of Venus, Mars, comet C/109P–Zhang 2001, Jupiter, and Saturn. Bottom panel, left, Saturn rings, middle, Earth, and right, Moon.

minor (heavy) ions in the solar wind and gaseous neutral species in the bodies' atmosphere.

This chapter surveys the current understanding of X-ray emission from the solar system bodies. We start our survey locally, at the Earth, move to the Moon and the nearby terrestrial planets, and then venture out to the giant planets and their moons. Next, we move to the small bodies, comets and asteroids, found between the planets, and finally we study the emission from the heliosphere surrounding the whole solar system. An overview is provided on the main source mechanisms of X-ray production at each object. For further detail, readers are referred to the bibliography provided at the end of the chapter and references therein.

2. Earth

2.1 Auroral Emissions

Precipitation of energetic charged particles from the magnetosphere into Earth's auroral upper atmosphere leads to ionization, excitation, dissociation, and heating of the neutral atmospheric gas. Deceleration of precipitating particles during their interaction with atoms and molecules in the atmosphere results in the production of continuous spectrum of X-ray photons, called bremsstrahlung (*bremstrahlung* is a German word for braking radiation). The main X-ray

production mechanism in the Earth's auroral zones, for energies above ~ 3 keV, is electron bremsstrahlung; therefore, the X-ray spectrum of the aurora has been found to be very useful in studying the characteristics of energetic electron precipitation. In addition, particles precipitating into the Earth's upper atmosphere give rise to discrete atomic emission lines in the X-ray range. The characteristic inner-shell line emissions for the main species of the Earth's atmosphere are all in the low-energy range (Nitrogen $K\alpha$ at 0.393 keV, Oxygen $K\alpha$ at 0.524 keV, Argon $K\alpha$ at 2.958 keV, and $K\beta$ at 3.191 keV). Very few X-ray observations have been made at energies where these lines emit.

While charged particles spiral around and travel along the magnetic field lines of the Earth, the majority of the X-ray photons in Earth's aurora are directed normal to the field, with a preferential direction toward the Earth at higher energies. Downward propagating X-rays cause additional ionization and excitation in the atmosphere below the altitude where the precipitating particles have their peak energy deposition. The fraction of the X-ray emission that is moving away from the ground can be studied using satellite-based imagers (e.g. AXIS on *UARS* and PIXIE on *POLAR* spacecraft).

Auroral X-ray bremsstrahlung has been observed from balloons and rockets since the 1960s and from spacecraft since the 1970s. Because of absorption of the low-energy

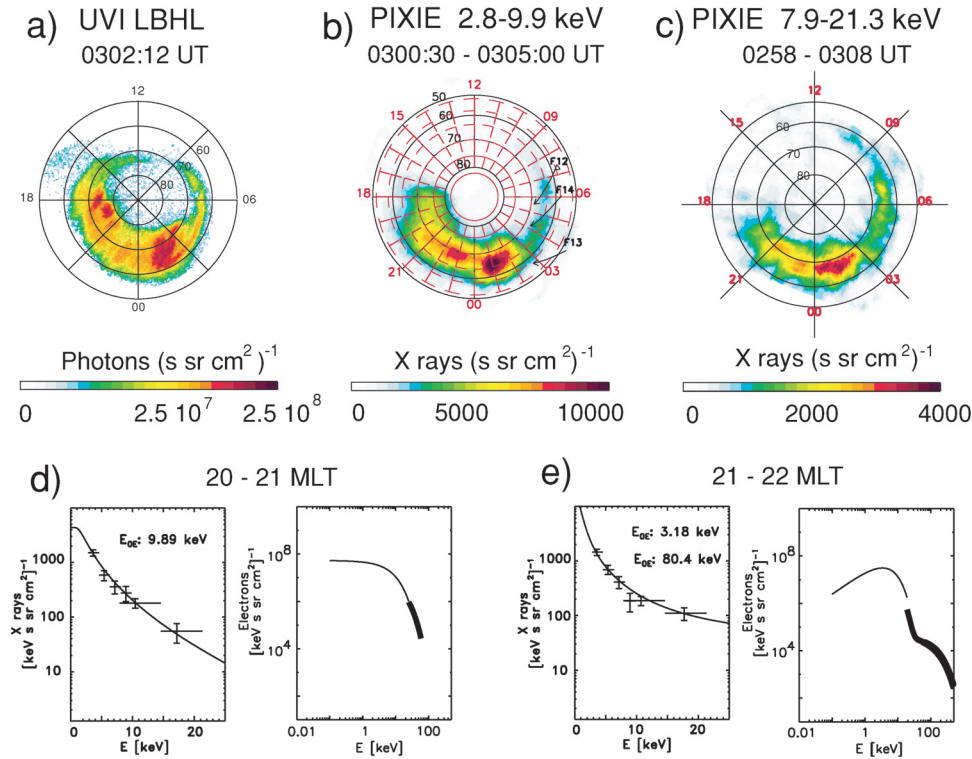


FIGURE 2 Earth's aurora. Polar satellite observation on July 31, 1987. (a) UVI and (b, c) PIXIE images in two different energy bands. (d) Left: The measured X-ray energy spectrum where an estimated X-ray spectrum produced by a single exponential electron spectrum with e-folding energy 9.89 keV is shown to be the best fit to the measurements. Right: The electron spectrum derived from UVI and PIXIE, where thin line is UVI contribution, thick line is PIXIE contribution. Both plots are averages within a box within 20–21 magnetic local time and 64° – 70° magnetic latitude. (e) Same as (d) but within 21–22 MLT, where X rays produced by a double exponential electron spectrum is shown to be the best fit to the X-ray measurements. (From Østgaard et al., *JGR*, 106, 26081, 2001.)

X-rays propagating from the production altitude (~ 100 km) down to balloon altitudes (35–40 km), such measurements were limited to >20 keV X-rays. Nevertheless, these early omnidirectional measurements of X-rays revealed detailed information of temporal structures from slowly varying bay events to fast pulsations and microburst.

The PIXIE instrument aboard *POLAR* is the first X-ray detector that provides true two-dimensional global X-ray image at energies >3 keV. In Fig. 2 two images taken by PIXIE in two different energy bands. The auroral X-ray zone can be clearly seen. Data from the PIXIE camera have shown that the X-ray bremsstrahlung intensity statistically peaks at midnight, is significant in the morning sector, and has a minimum in the early dusk sector. During solar substorms X-ray imaging shows that the energetic electron precipitation brightens up in the midnight sector and has a prolonged and delayed maximum in the morning sector due to the scattering of magnetic-drifting electrons and shows an evolution significantly different than viewing in the UV emissions.

During the onset/expansion phase of a typical substorm the electron energy deposition power is about 60–90 GW, which produces 10–30 MW of bremsstrahlung X-rays. By combining the results of PIXIE with the UV imager aboard *POLAR*, it has been possible to derive the energy distribution of precipitating electrons in the 0.1–100 keV range with a time resolution of about 5 min (see Fig. 2). Because these energy spectra cover the entire energy range important for

the electrodynamics of the ionosphere, important parameters like Hall and Pedersen conductivity and Joule heating can be determined on a global scale with larger certainties than parameterized models can do. Electron energy deposition estimated from global X-ray imaging also give valuable information on how the constituents of the upper atmosphere, like NO_x , is modified by energetic electron precipitation.

Limb scans of the nighttime Earth at low- to mid-latitude by the X-ray astronomy satellite *HEAO-1* in 1977, in the energy range 0.15–3 keV, showed clear evidence of the $\text{K}\alpha$ lines for nitrogen and oxygen sitting on top of the bremsstrahlung spectrum. Recently, the High-Resolution Camera (HRC-I) aboard the *Chandra* X-ray Observatory imaged the northern auroral regions of the Earth in the 0.1- to 10-keV X-ray range at 10 epochs (each ~ 20 min duration) between December 2003 and April 2004. These first soft X-ray observations of Earth's aurora (see Fig. 3) showed that it is highly variable (intense arcs, multiple arcs, diffuse patches, at times absent). Also, one of the observations showed an isolated blob of emission near the expected cusp location. Modeling of the observed soft X-ray emissions suggests that it is a combination of bremsstrahlung and characteristic K-shell line emissions of nitrogen and oxygen in the atmosphere produced by electrons. In the soft X-ray energy range of 0.1–2 keV, these line emissions are ~ 5 times more intense than the X-ray bremsstrahlung.

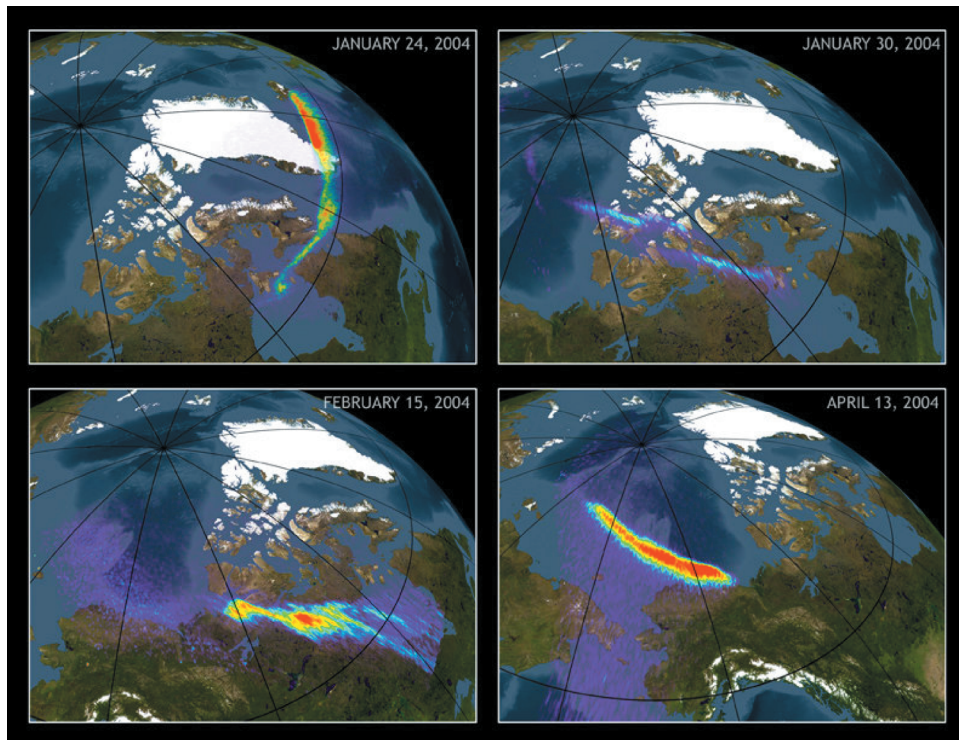


FIGURE 3 Earth's aurora. Four X-rays images (shown on the same brightness scale) of the north polar regions of Earth obtained by *Chandra* HRC-I on different days (marked at the top of each image), showing large variability in soft (0.1–10.0 keV) X-ray emissions from Earth's aurora. The bright arcs in these *Chandra* images show low-energy X-rays generated during auroral activity. The images—seen here superimposed on a simulated image of Earth—are from an approximately 20-minute scan during which *Chandra* was pointed at a fixed point in the sky while the Earth's motion carried the auroral region through the field of view. Distance from the North Pole to the black circle is 3,340 km. (From Bhardwaj et al., 2006, *J. Atmos. Sol-Terr. Phys.*, and http://chandra.harvard.edu/press/05_releases/press_122805.html.)

2.2 Nonauroral Emissions

The nonauroral X-ray background above 2 keV from the Earth is almost completely negligible except for brief periods during major solar flares. However, at energies below 2 keV, soft X-rays from the sunlit Earth's atmosphere have been observed even during quiet (nonflaring) Sun conditions. The two primary mechanisms for the production of X-rays from the sunlit atmosphere are: (1) Thomson (coherent) scattering of solar X-rays from the electrons in the atomic and molecular constituents of the atmosphere, and (2) the absorption of incident solar X-rays followed by the resonance fluorescence emission of characteristic K lines of nitrogen, oxygen, and argon. During flares, solar X-rays light up the sunlit side of the Earth by Thomson and fluorescent scattering; the X-ray brightness can be comparable to that of a moderate aurora.

Around 1994, the Compton Gamma Ray Observatory (CGRO) satellite detected a new type of X-ray source from the Earth. These are very short-lived (1 ms) X-ray and γ -ray bursts (~ 25 keV to 1 MeV) from the atmosphere above thunderstorms, whose occurrence is also supported by the more recent Reuvan Ramaty High Energy Solar Spectroscopic Imager (RHESSI) observations. It has been suggested that these emissions are bremsstrahlung from upward-propagating, relativistic (MeV) electrons generated in a runaway electron discharge process above thunderclouds by the transient electric field following a positive cloud-to-ground lightning event.

3. The Moon

X-Ray emissions from the Earth's nearest planetary body, the Moon, have been studied in two ways: close up from lunar orbiters (e.g., *Apollo 15* and *16*, *Clementine*, and *SMART-1*), and more distantly from Earth-orbiting X-ray astronomy telescopes (e.g., *ROSAT* and *Chandra*). Lunar X-rays result mainly from fluorescence of sunlight by the surface, in addition to a low level of scattered solar radiation and a very low level of bremsstrahlung from solar wind electrons impacting the surface. Thus, X-ray fluorescence studies provide an excellent way to determine the elemental composition of the lunar surface by remote sensing, since at X-ray wavelengths the optical properties of the surface are dominated by its elemental abundances. Elemental abundance maps produced by the X-ray spectrometers on the *Apollo 15* and *16* orbiters were limited to the equatorial regions but succeeded in finding geochemically interesting variations in the relative abundances of Al, Mg, and Si. Although the energy resolution of the *Apollo* proportional counters was low, important results were obtained, such as the enhancement of Al/Si in the lunar highlands relative to the mare. Recently, the D-CIXS instrument on *SMART-1* has obtained abundances of Al, Si, Fe, and even Ca at 50-km resolution from a 300-km altitude orbit about the Moon. Upcoming missions planned for launch in 2007–2008 by Japan (*SELENE*), India (*Chandrayaan-1*), and China (*Chang'e*) will each carry X-ray spectrometers to obtain further improved maps of the Moon's elemental

composition, at ~ 20 -to 50 -km resolution from ~ 100 - to 200 -km altitude polar orbits.

Early observations from Earth orbit were made using the *ROSAT*. A marginal detection by the Advanced Satellite for Cosmology and Astrophysics (ASCA) is also reported. Figure 4a shows the *ROSAT* images of the Moon, the right image is data from a lunar occultation of the bright X-ray source GX5-1. The power of the reflected and fluoresced X-rays observed by *ROSAT* in the 0.1 - to 2 -keV range coming from the sunlit surface was determined to be only 73 kW. The faint but distinct lunar night side emissions (100 times less bright than the day side emissions) were until recently a matter of controversy. Earlier suggestions had the night side X-rays produced by bremsstrahlung of solar wind electrons of several hundred eV impacting the night side of the Moon on its evening (leading) hemisphere. However, this was before the GX5-1 data were acquired, which clearly show lunar night side X-rays from the early morning (trailing) hemisphere as well. A new, much better and accepted explanation is that the heavy ions in the solar wind charge exchange with geocoronal and interstellar H atoms that lie between the Earth and Moon resulting in foreground X-ray emissions between *ROSAT* and the Moon's dark side. This was confirmed by *Chandra* ACIS observations in 2001 (see Fig. 4c).

The July 2001 *Chandra* observations also provide the first remote measurements that clearly resolve discrete K-shell fluorescence lines of O, Mg, Al, and Si on the sunlit side of the Moon (see Fig. 4b). The observed O-K line photons correspond to a flux of 3.8×10^{-5} photons/s/cm²/arcmin² (3.2×10^{-14} erg/s/cm²/arcmin²). The Mg-K, Al-K, and Si-K lines each had roughly 10% as many counts and 3% as much flux as O-K line, but statistics were inadequate to draw any conclusions regarding differences in element abundance ratios between highlands and maria. More recent *Chandra* observations of the Moon used the photon counting, high spatial resolution HRC-I imager to look for albedo variations due to elemental composition differences between highlands and maria. The observed albedo contrast was noticeable, but very slight, making remote elemental mapping difficult.

4. Venus

The first X-ray observation of Venus was obtained by *Chandra* in January 2001. It was expected that Venus would be an X-ray source due to two processes: (1) charge exchange interactions between highly charged ions in the solar wind and the Venusian atmosphere and (2) scattering of solar X-rays in the Venusian atmosphere. The predicted X-ray luminosities were ~ 0.1 – 1.5 MW for the first process, and ~ 35 MW for the second one, with an uncertainty factor of about two. The *Chandra* observation of 2001 consisted of two parts: grating spectroscopy with LETG/ACIS-S and

direct imaging with ACIS-I. This combination yielded data of high spatial, spectral, and temporal resolution. Venus was clearly detected as a half-lit crescent, exhibiting considerable brightening on the sunward limb (Fig. 5); the LETG/ACIS-S data showed that the spectrum was dominated by O-K α and C-K α emission, and both instruments indicated temporal variability of the X-ray flux. An average luminosity of 55 MW was found, which agreed well with the theoretical predictions for scattered solar X-rays. In addition to the C-K α and O-K α emission at 0.28 and 0.53 keV, respectively, the LETG/ACIS-S spectrum also showed evidence for N-K α emission at 0.40 keV. An additional emission line was indicated at 0.29 keV, which might be the signature of the C $1s \rightarrow \pi^*$ transition in CO₂. The observational results are consistent with fluorescent scattering of solar X-rays by the majority species in the Venusian atmosphere, and no evidence of the 30 times weaker charge exchange interactions was found. Simulations showed that fluorescent scattering of solar X-rays is most efficient in the Venusian upper atmosphere at heights of ~ 120 km, where an optical depth of one is reached for incident X-rays with energy 0.2 – 0.9 keV.

The appearance of Venus is different in optical light and X-rays. The reason for this is that the optical light is reflected from clouds at a height of 50 – 70 km, while scattering of X-rays takes place at higher regions extending into the tenuous, optically thin parts of the thermosphere and exosphere. As a result, the Venusian sun-lit hemisphere appears surrounded by an almost transparent luminous shell in X-rays, and Venus looks brightest at the limb because more luminous material is there. Because X-ray brightening depends sensitively on the density and chemical composition of the Venusian atmosphere, its precise measurement will provide direct information about the atmospheric structure in the thermosphere and exosphere. This opens up the possibility of using X-ray observations for monitoring the properties of these regions that are difficult to investigate by other means, as well as their response to solar activity. In 2007, *Chandra* will reobserve Venus during its best window for 2 years, while the *MESSENGER* spacecraft, flying by on its way to Mercury, and the *Venus Express* spacecraft in Venusian orbit probe the temperature, density, pressure, and composition of the Venusian atmosphere.

5. Mars

The first X-rays from Mars were detected on 4 July 2001 with the ACIS-I detector onboard *Chandra*. In the *Chandra* observations, Mars showed up as an almost fully illuminated disk (Fig. 6). An indication of limb brightening on the sunward side, accompanied by some fading on the opposite side, was observed. The observed morphology and X-ray luminosity of ~ 4 MW, about 10 times less than at Venus,

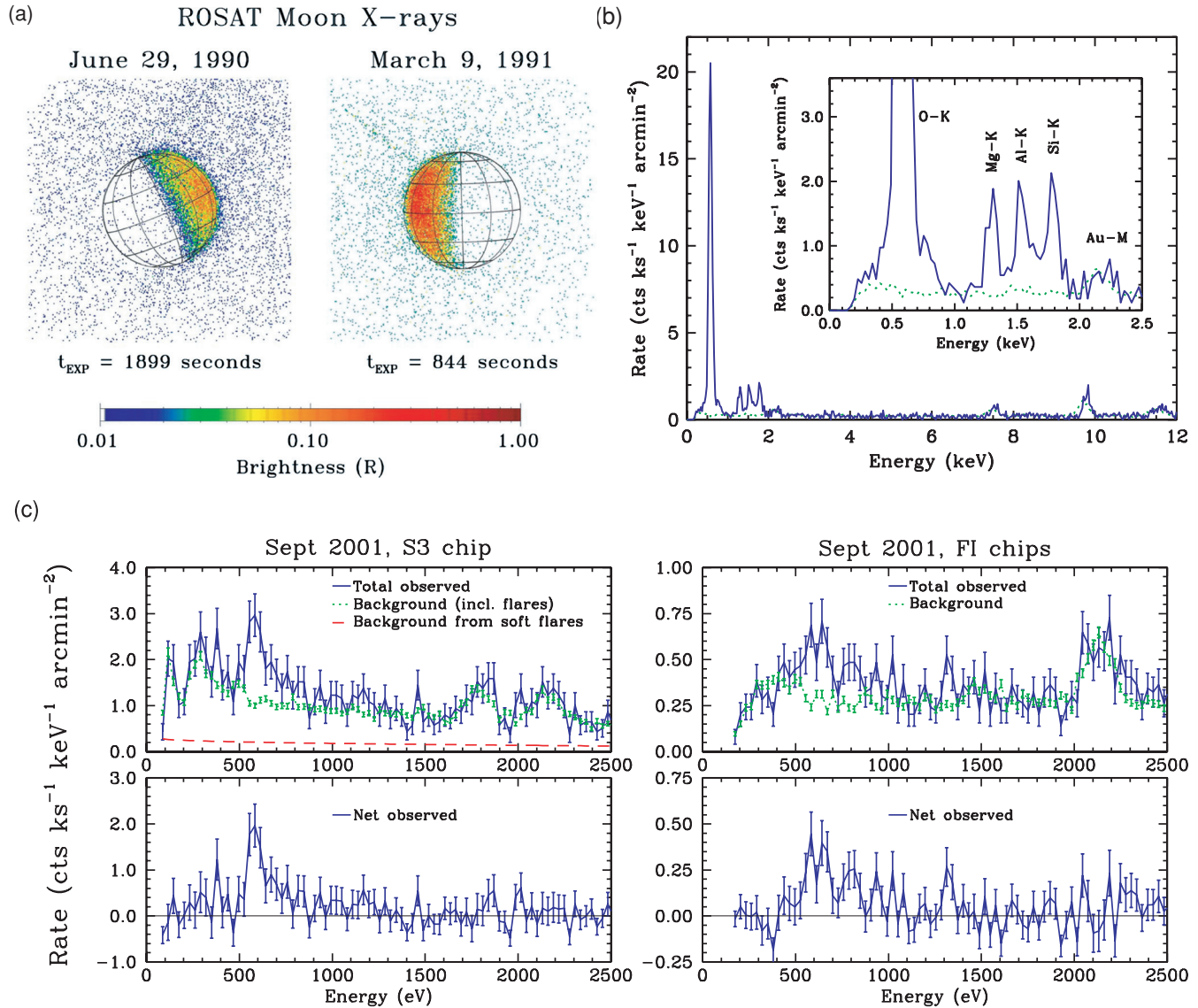
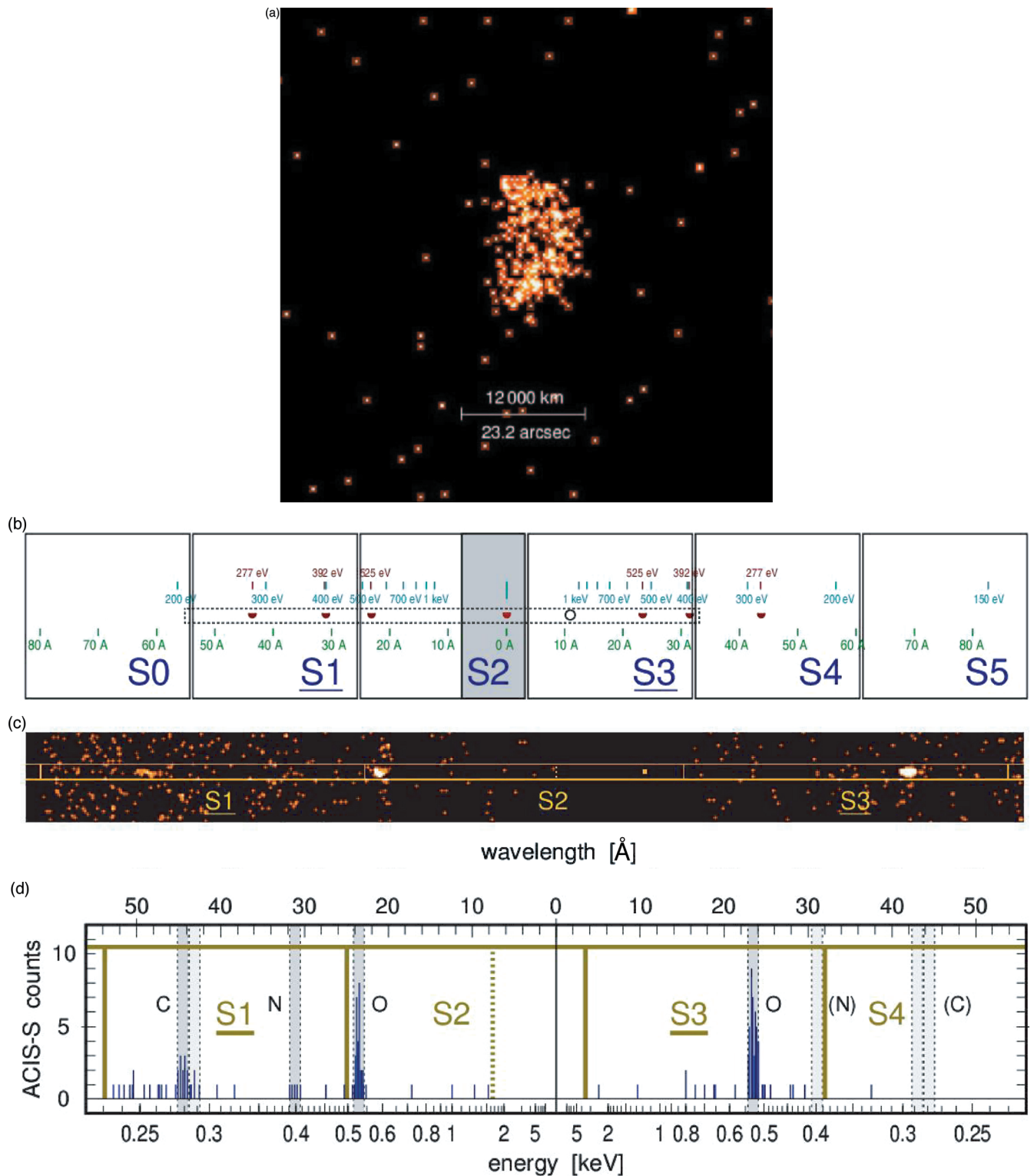


FIGURE 4 The Moon. (a) *ROSAT* soft X-ray (0.1–2 keV) images of the Moon at first (left side) and last (right side) quarter. The day side lunar emissions are thought to be primarily reflected and fluoresced sunlight, while the faint night side emissions are foreground due to charge exchange of solar wind heavy ions with H atoms in Earth’s exosphere. The brightness scale in R assumes an average effective area of 100 cm² for the *ROSAT* *PSPC* over the lunar spectrum. [From Bhardwaj et al., 2002, *ESA-SP-514*, 215–226.] (b) *Chandra* spectrum of the bright side of the Moon. The green dotted curve is the detector background. K-shell fluorescence lines from O, Mg, Al, and Si are shifted up by 50 eV from their true values because of residual optical leak effects. Features at 2.2, 7.5, and 9.7 keV are intrinsic to the detector. [From Wargelin et al., 2004, *Astrophys. J.*, **607**, 596–610.] (c) Observed and background-subtracted spectra from the September 2001 *Chandra* observation of the dark side of the Moon, with 29-eV binning. Left panel is from the higher-QE but lower-resolution ACIS S3 CCD; right panel shows the higher resolution ACIS front-illuminated (FI) CCDs. Oxygen emission from charge exchange is clearly seen in both spectra, and energy resolution in the FI chips is sufficient that O Lyman α is largely resolved from O $K\alpha$. High- n H-like O Lyman lines are also apparent in the FI spectrum, along with what is likely Mg $K\alpha$ around 1340 eV. (From Wargelin et al., 2004, *Astrophys. J.*, **607**, 596–610.)



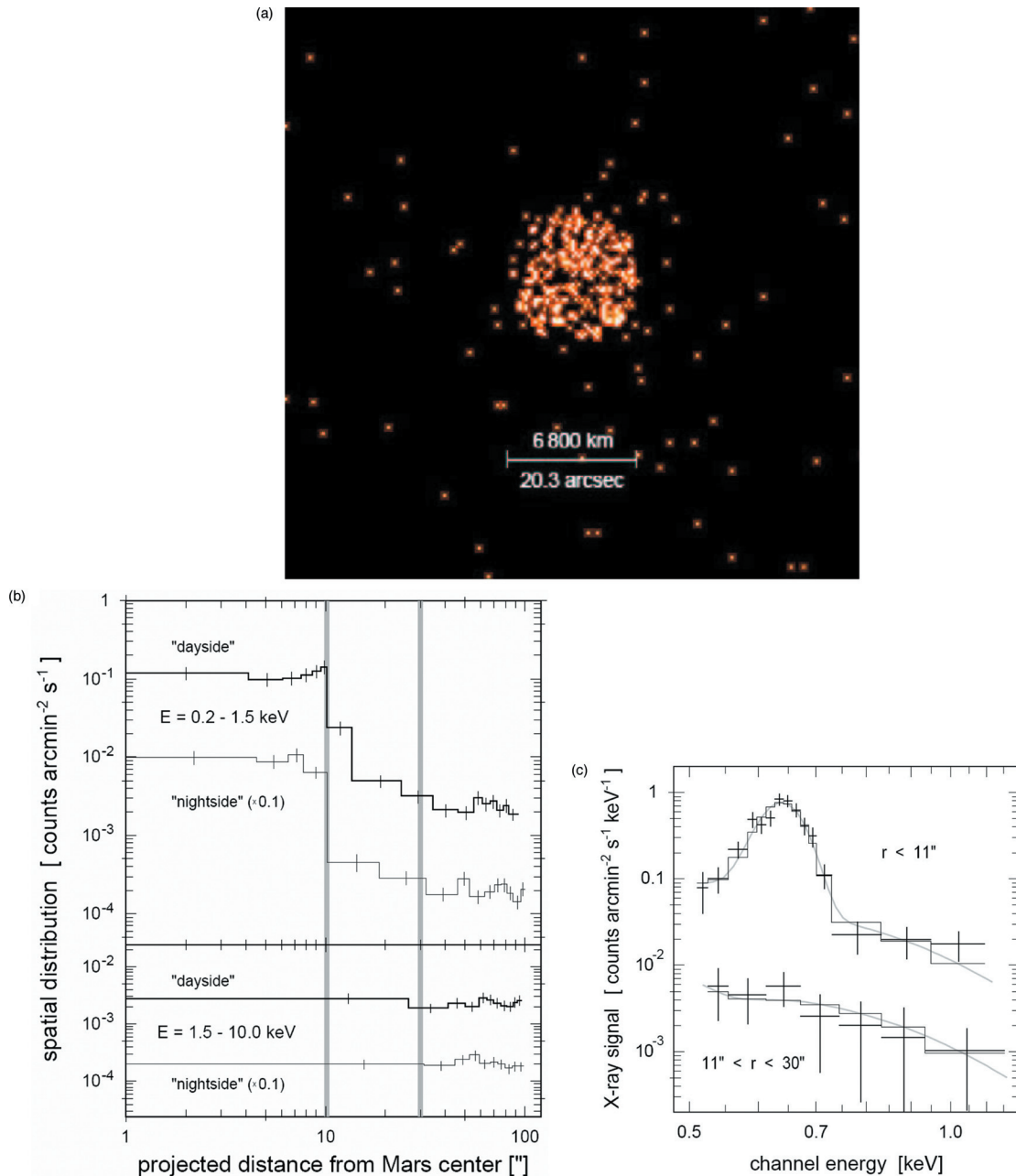


FIGURE 6 Mars. (a) First X-ray image of Mars, obtained with *Chandra* ACIS-I. The X-rays result mainly from fluorescent scattering of solar X-rays on C and O in the upper Mars atmosphere, at heights of 110–130 km, similar to Venus. The X-ray glow of the Martian exosphere is too faint to be directly visible in this image. (From Dennerl, 2002, *Astronomy and Astrophysics*, **394**, 1119–1128.) (b) Spatial distribution of the photons around Mars in the soft ($E = 0.2 - 1.5$ keV) and hard ($E = 1.5 - 10.0$ keV) energy range, in terms of surface brightness along radial rings around Mars, separately for the day side (offset along projected solar direction >0) and the night side (offset <0); note, however, that the phase angle was only 18.2° . For better clarity the night side histograms were shifted by one decade downward. The bin size was adaptively determined so that each bin contains at least 28 counts. The thick vertical lines enclose the region between one and three Mars radii. (c) X-Ray spectra of Mars (top) and its X-ray halo (bottom). Crosses with $1-\sigma$ error bars show the observed spectra; the model spectra, convolved with the detector response, are indicated by gray curves (unbinned) and by histograms (binned as the observed spectra). The spectrum of Mars itself is characterized by a single narrow emission line (this is most likely the O-K α fluorescence line at 0.53 keV (the apparent displacement of the line energy is due to optical loading)). At higher energies, the presence of an additional spectral component is indicated. The spectral shape of this component can be well modeled by the same 0.2 keV thermal bremsstrahlung emission which describes the spectrum of the X-ray halo. (From Dennerl, 2002, *Astron. Astrophys.*, **394**, 1119–1128.)

was consistent with fluorescent scattering of solar X-rays in the upper Mars atmosphere. The X-ray spectrum was dominated by a single narrow emission line caused by O $K\alpha$ fluorescence.

Simulations suggest that scattering of solar X-rays is most efficient between 110 km (along the subsolar direction) and 136 km (along the terminator) above the Martian surface. This behavior is similar to that seen on the Venus. No evidence for temporal variability or dust-related emission was found, which is in agreement with fluorescent scattering of solar X-rays as the dominant process responsible for the Martian X-ray. A gradual decrease in the X-ray surface brightness between 1 and ~ 3 Mars radii is observed (see Fig. 6). Within the limited statistical quality of the low flux observations, the spectrum of this region (halo) resembled that of comets: suggesting that they are caused by charge exchange interactions between highly charged heavy ions in the solar wind and neutrals in the Martian exosphere (corona). For the X-ray halo observed within 3 Mars radii, excluding Mars itself, the *Chandra* observation yielded a flux of about 1×10^{-14} erg cm $^{-2}$ s $^{-1}$ in the energy range 0.5–1.2 keV, corresponding to a luminosity of 0.5 ± 0.2 MW for isotropic emission, which agrees well with that expected theoretically for solar wind charge exchange mechanism.

The first *XMM-Newton* observation of Mars in November 2003 confirmed the presence of the Martian X-ray halo and made a detailed analysis of its spectral, spatial, and temporal properties. High-resolution spectroscopy of the halo with *XMM-Newton* RGS revealed the presence of numerous (~ 12) emission lines at the positions expected for deexcitation of highly ionized C, N, O, and Ne atoms, the dominant atomic species in the Martian atmosphere. The He-like O multiplet was resolved and found to be dominated by the spin-forbidden magnetic dipole transition $2^3S_1 \rightarrow 1^1S_0$, confirming that charge exchange process is at the origin of the emission. This was the first definite detection of charge exchange induced X-ray emission from the exosphere of another planet.

The *XMM-Newton* observation confirmed that the fluorescent scattering of solar X-rays from the Martian disk is clearly concentrated on the planet, and is directly correlated with the solar X-ray flux levels. On the other hand, the Martian X-ray halo was found to extend out to ~ 8 Mars radii, with pronounced morphological differences between individual ions and ionization states. While the emission from ionized oxygen (Fig. 7c) appears to be concentrated in two distinct blobs a few thousand kilometers above the Martian poles, with larger heights for O $^{7+}$ than for O $^{6+}$, the emissions from ionized carbon (Fig. 7f) exhibit a more band-like structure without a pronounced intensity dip at the position of Mars. The halo emission exhibited pronounced variability, but, as expected for solar wind interactions, the variability of the halo did not show any correlation with the solar X-ray flux.

6. Jupiter

6.1 Auroral Emission

Like the Earth, Jupiter emits X-rays both from its aurora and its sunlit disk. Jupiter's ultraviolet auroral emissions were first observed by the *International Ultraviolet Explorer (IUE)* and soon confirmed by the *Voyager 1* Ultraviolet Spectrometer as it flew through the Jupiter system in 1979 (see Bhardwaj and Gladstone, 2000 for review). The first detection of the X-ray emission from Jupiter was also made in 1979; the satellite-based Einstein observatory detected X-rays in the 0.2–3.0 keV energy range from both poles of Jupiter, due to the aurora. Analogous to the processes on Earth, it was expected that Jupiter's X-rays might originate as bremsstrahlung by precipitating electrons. However, the power requirement for producing the observed emission with this mechanism (10^{15} – 10^{16} W) is more than two orders of magnitude larger than the input auroral power available as derived from *Voyager* and *IUE* observations of the ultraviolet aurora. (The strong Jovian magnetic field excludes the bulk of the solar wind from penetrating close to Jupiter, and the solar wind at Jupiter at 5.2 AU is 27 times less dense than at the Earth at 1 AU.) Precipitating energetic sulfur and oxygen ions from the inner magnetosphere, with energies in the 0.3–4.0 MeV/nucleon range, was suggested as the source mechanism responsible for the production of X-rays on Jupiter. The heavy ions are thought to start as neutral SO and SO $_2$ emitted by the volcanoes on Io into the jovian magnetosphere, where they are ionized by solar UV radiation, and then swept up into the huge dynamo created by Jupiter's rotating magnetic field. The ions eventually become channeled onto magnetic field lines terminating at Jupiter's poles, where they emit X-rays by first charge stripping to a highly ionized state, followed by charge exchange and excitation through collisions with H $_2$.

ROSAT's observations of Jupiter X-ray emissions supported this suggestion. The spatial resolution of these early observations was not adequate to distinguish whether the emissions were linked to source regions near the Io torus of Jupiter's magnetosphere (inner magnetosphere) or at larger radial distances from the planet. The advent of *Chandra* and *XMM-Newton* X-ray observatories revolutionized our thinking about Jupiter's X-ray aurora. High-spatial resolution (< 1 arcsec) observations of Jupiter with the *Chandra* in December 2000 (see Fig. 8) revealed that most of Jupiter's northern auroral X-rays come from a "hot spot" located significantly poleward of the UV auroral zones (20 – $30 R_J$), and not at latitudes connected to the inner magnetosphere. The hot spot is fixed in magnetic latitude (60 – 70°) and longitude (160 – 180° system III longitude) and occurs in a region where anomalous infrared and ultraviolet emissions (the so-called flares) have also been observed. On the other hand, auroral X-rays from the south (70 – 80° S latitude) spread almost halfway across the planet (~ 300 – 360° and 0 – 120°

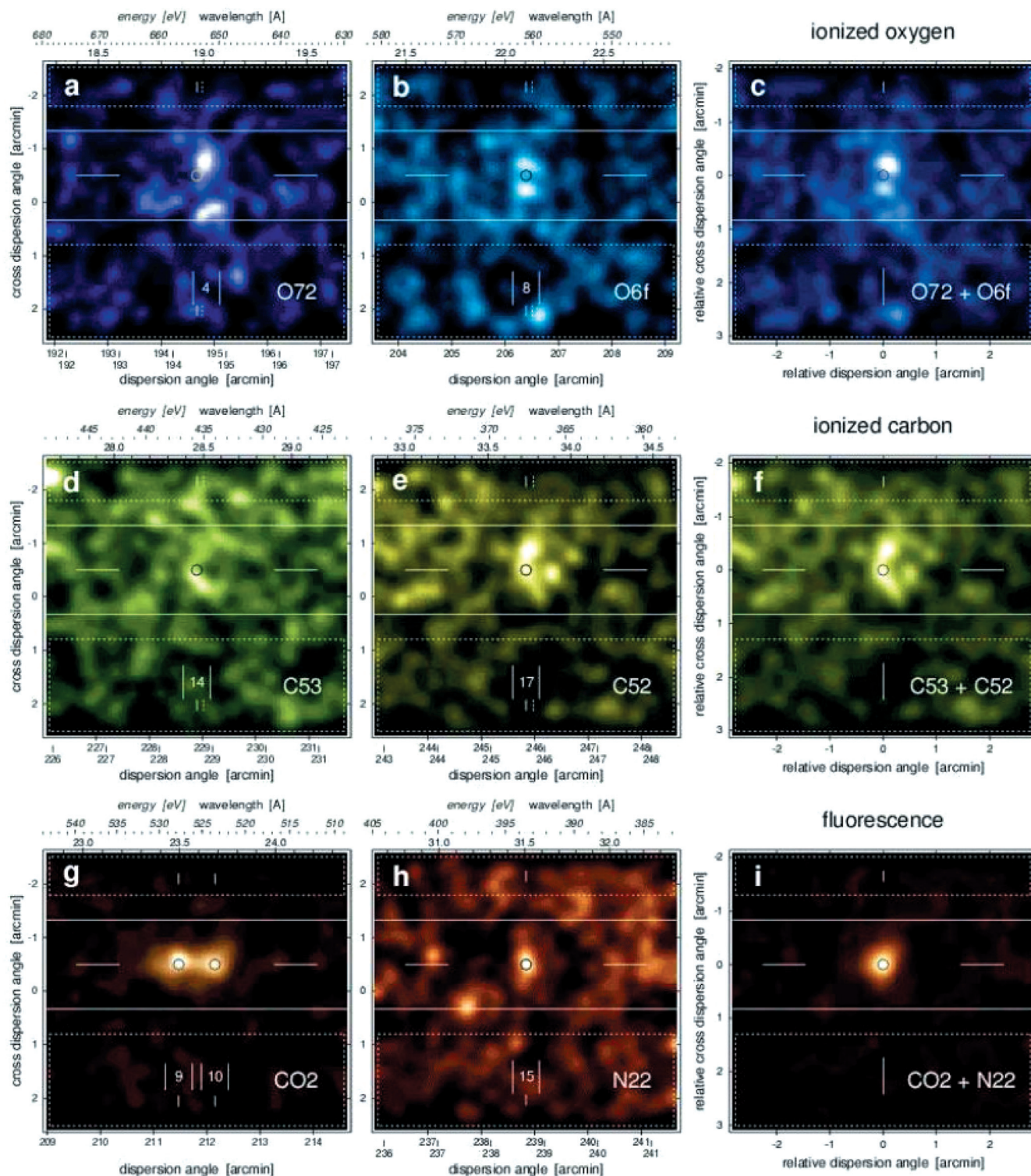


FIGURE 7 Mars. XMM-Newton's RGS images of Mars and its halo in the individual emission lines of ionized oxygen (top row), ionized carbon (middle row), and fluorescence of CO₂ and N₂ molecules (bottom row). The images were corrected for exposure variations, were binned into 2"×2" pixels and smoothed with a Gaussian function with $\sigma = 8'' \times 8''$. All are displayed at the same angular scale; the dynamic scale, however, was individually adjusted. (From Dennerl et al., 2006, *Astron. Astrophys.*, **451**, 709–722)

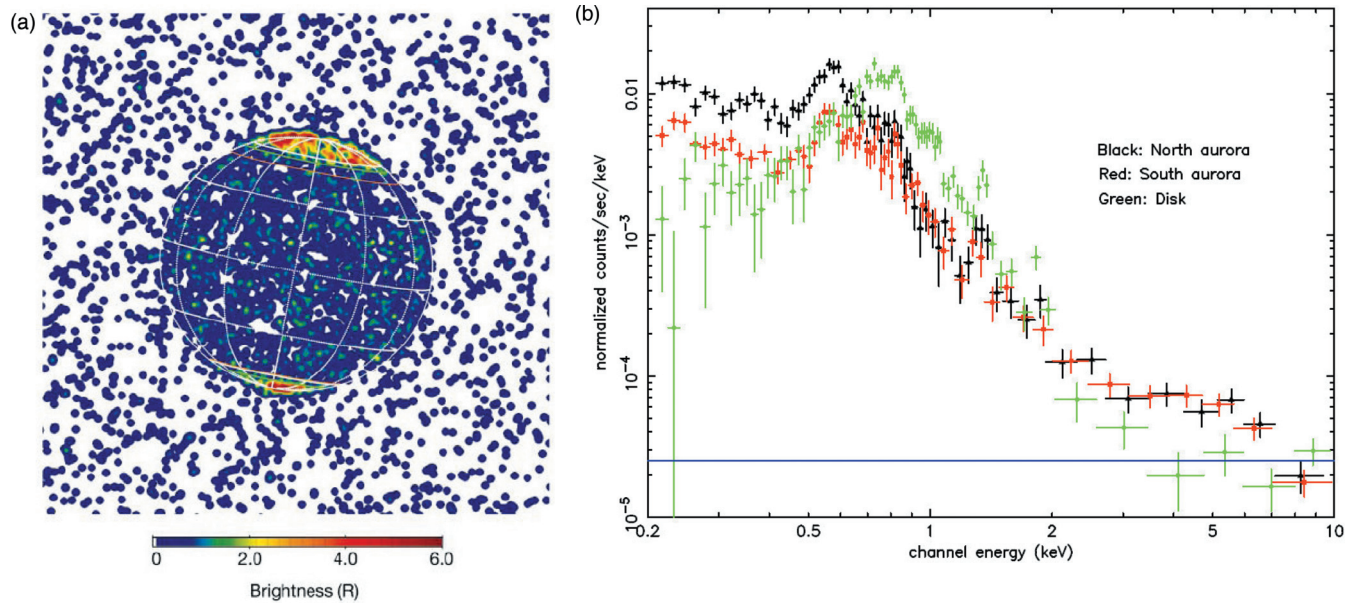


FIGURE 8 Jupiter. (a) Detailed X-ray morphology first obtained with *Chandra* HRC-I on 18 Dec. 2000, showing bright X-ray emission from the polar ‘auroral’ regions, indicating the high-latitude position of the emissions, and a uniform distribution from the low-latitude ‘disk’ regions. [from Gladstone et al., *Nature*, 415, 1000, 2002]. (b) Combined XMM-Newton EPIC spectra from the Nov. 2003 observation of Jupiter. Data points for the North and South aurorae are in black and red respectively. In green is the spectrum of the low-latitude disk emission. Differences in spectral shape between auroral and disk spectra are clear. The presence of a high energy component in the spectra of the aurorae is very evident, with a substantial excess relative to the disk emission extending to 7 keV. The horizontal blue line shows the estimated level of the EPIC particle background. [from Branduardi-Raymont et al., *ESA SP-604*, Vol. 1, pp. 15–20, 2006].

longitude). The location of the auroral X-rays connects along magnetic field lines to regions in the jovian magnetosphere well in excess of 30 jovian radii from the planet, a region where there are insufficient S and O ions to account for the X-ray emission. Acceleration of energetic ions was invoked to increase the phase space distribution, but now the question was whether the acceleration involved outer magnetospheric heavy ions or solar wind heavy ions.

Surprisingly, *Chandra* observations also showed that X-rays for jovian aurora pulsate with a periodicity that is quite systematic (approximately 45-min period) at times (in December 2000) and irregular (20–70 min range) at other times (in February 2003). The 45-min periodicity is highly reminiscent of a class of Jupiter high-latitude radio emissions known as quasi-periodic radio bursts, which had been observed by *Ulysses* in conjunction with energetic electron acceleration in Jupiter’s outer magnetosphere. During the 2003 *Chandra* observation of Jupiter, the *Ulysses* radio data did not show any strong 45-min quasi-periodic oscillations, although variability on time scales similar to that in X-rays was present. *Chandra* also found that X-rays from the north and south auroral regions are neither in phase nor in antiphase, but that the peaks in the south are shifted from those in the north by about 120° (i.e., one-third of a planetary rotation).

A clear temporal association of the X-ray emission intensity with a jovian UV flare has been observed during a simultaneous *Hubble Space Telescope* and *Chandra* observation in February 2003. However, the spatial correlation was not as expected. The X-rays did increase in time in a manner consistent with the ultraviolet flare, but rather than peak at the ultraviolet flare location they were peaked in a morphologically associated region, the “kink,” which most likely magnetically maps to the dusk flank of Jupiter’s magnetosphere.

The *Chandra* and XMM-Newton spectral observations have now established that soft (~ 0.1 –2 keV) X-rays from jovian aurora are line emissions, which are consistent with high-charge states of precipitating heavy (C, O, S) ions, and not a continuum as might be expected from electron bremsstrahlung (see Fig. 8). XMM-Newton has provided spectral information on the X-rays from Jupiter, which is somewhat better than *Chandra*. The RGS on XMM-Newton clearly resolves the strongest lines in the spectra, while the EPIC camera has provided images of the planets in the strong OVII and OVIII lines present in the jovian auroral emissions. The spectral interpretation of *Chandra* and XMM-Newton observations is consistent with a source due to energetic ion precipitation that undergoes acceleration to attain energies of > 1 MeV/nucleon before impacting the

jovian upper atmosphere. This is also supported by modeling studies.

Recently, *XMM-Newton* and *Chandra* data have suggested that there is a higher (>2 keV) energy component present in the spectrum of Jupiter's aurora; they found it to be variable on timescales of days. The observed spectrum and flux, at times, appears consistent with that predicted from bremsstrahlung of energetic electrons precipitating from the magnetosphere, but at energies greater than 2 keV (at lower energies bremsstrahlung still fall short by an order of magnitude). The variability suggests a link to changes in the energy distribution of the precipitating magnetospheric electrons and may be related to the solar activity at the time of observation.

6.2 Nonauroral (Disk) Emission

The existence of low-latitude “disk” X-ray emission from Jupiter was first recognized in *ROSAT* observations made in 1994. These X-rays were initially thought to be the result of precipitation of energetic S and O ions from Jupiter's inner radiation belts into the planet's atmosphere. Later, as for the inner planets, it was suggested that elastic scattering of solar X-rays by atmospheric neutrals (H_2) and fluorescent scattering of carbon K-shell X-rays from CH_4 molecules located below the jovian homopause was the source of the disk X-rays.

A general decrease in the overall X-ray brightness of Jupiter observed by *ROSAT* over the years 1994–1996 was found to be coincident with a similar decay in solar activity index (solar 10.7 cm flux). A similar trend is seen in the data obtained by *Chandra* in 2000 and 2003; Jupiter disk was about 50% dimmer in 2003 compared to that in 2000, which is consistent with variation in the solar activity index. First direct evidence for temporal correlation between jovian disk X-rays and solar X-rays is provided by *XMM-Newton* observations of Jupiter in November 2003, which demonstrated that day-to-day variation in disk X-rays of Jupiter are synchronized with variation in the solar X-ray flux, including a solar flare that has a matching feature in the jovian disk X-ray light curve. *Chandra* observations of December 2000 and February 2003 also support this association between light curves of solar and planetary X-rays. However, there is an indication of higher X-ray counts from regions of low surface magnetic field in the *Chandra* data, suggesting the presence of some particle precipitation.

The higher spatial resolution observation by *Chandra* has shown that nonauroral disk X-rays is relatively more spatially uniform than the auroral X-rays (Fig. 8). Unlike the $\sim 40 \pm 20$ -min quasi-periodic oscillations seen in auroral X-ray emission, the disk emission does not show any systematic pulsations. There is a clear difference between the X-ray spectra from the disk and auroral region on Jupiter; the disk spectrum peaks at higher energies (0.7–0.8 keV)

than the aurorae (0.5–0.6 keV) and lacks the high-energy component (above ~ 3 keV) present in the latter (see Fig. 8).

7. Galilean Satellites

The jovian *Chandra* observations on 25–26 November 1999 and 18 December 2000 discovered X-ray emission from the Galilean satellites (Fig. 9). These satellites are very faint when observed from Earth orbit (by *Chandra*), and the detections of Io and Europa, although statistically very significant, were based on ~ 10 photons each! The energies of the detected X-ray events ranged between 300 and 1890 eV and appeared to show a clustering between 500 and 700 eV, suggestive of oxygen K-shell fluorescent emission. The estimated power of the X-ray emission was 2 MW for Io and 3 MW for Europa. There were also indications of X-ray emission from Ganymede. X-ray emission from Callisto seems likely at levels not too far below the CXO sensitivity limit because the magnetospheric heavy ion fluxes are an order of magnitude lower than at Ganymede and Europa, respectively.

The most plausible emission mechanism is inner (K shell) ionization of the surface (and incoming magnetospheric) atoms followed by prompt X-ray emission. Oxygen should be the dominant emitting atom either in an SiO_x (silicate) or SO_x (sulfur oxides) surface (Io) or on an icy one (the outer Galilean satellites). It is also the most common heavy ion in the jovian magnetosphere. The extremely tenuous atmospheres of the satellites are transparent to X-ray photons with these energies, as well as to much of the energy range of the incoming ions. However, oxygen absorption in the soft X-ray is strong enough that the X-rays must originate within the top 10 micrometers of the surface in order to escape. Simple estimates suggest that excitation by incoming ions dominates over electrons and that the X-ray flux produced is within a factor of 3 of the measured flux. The detection of X-ray emission from the Galilean satellites thus provides a direct measure of the interactions of the magnetosphere of Jupiter with the satellite surfaces. An intriguing possibility is placement of an imaging X-ray spectrometer on board a mission to the Jupiter system. If such an instrument was in orbit around a Galilean satellite (e.g., Europa or Ganymede), even though it would be immersed in a fierce radiation environment, it would be able to map the elemental abundances of the surface for elements from C through Fe.

8. Io Plasma Torus

The Io Plasma Torus (IPT) is known to emit at extreme ultraviolet (EUV) energies and below, but it was a surprise when *Chandra* discovered that it was also a soft X-ray source. The 1999 jovian *Chandra* observations

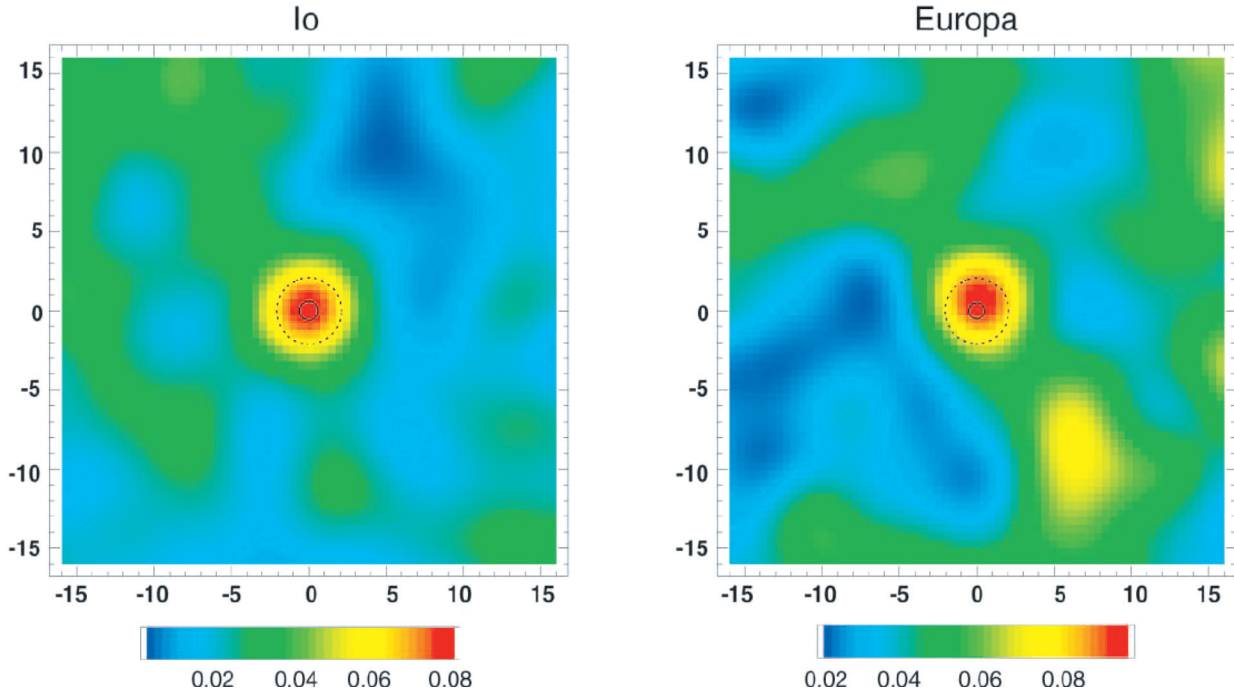


FIGURE 9 Galilean Moons. Chandra X-ray images of Io and Europa ($0.25 \text{ keV} < E < 2.0 \text{ keV}$) from November, 1999 observations. The images have been smoothed by a two-dimensional gaussian with $\sigma = 2.46 \text{ arcsec}$ (5 detector pixels). The axes are labeled in arcsec (1 arcsec $\approx 2995 \text{ km}$) and the scale bar is in units of smoothed counts per image pixel (0.492 by 0.492 arcsec). The solid circle shows the size of the satellite (the radii of Io and Europa are 1821 km and 1560 km, respectively), and the dotted circle the size of the detect cell. [from Elsner et al., *Astrophysical Journal*, 572, 1077–1082, 2002].

detected a faint diffuse source of soft X-rays from the region of the IPT. The 2000 *Chandra* image, obtained with the HRC-I camera (Fig. 10), exhibited a dawn-to-dusk asymmetry similar to that seen in the EUV. Figure 10 shows the background-subtracted *Chandra*/ACIS-S IPT spectrum for 25–26 November 1999. This spectrum shows evidence for line emission centered on 574 eV (very near a strong O VII line), together with a very steep continuum spectrum at the softest X-ray energies. Although formed from the same source, the spectrum is different than from the jovian aurora because the energies, charge states, and velocities of the ions in the torus are much lower—the bulk ions have not yet been highly accelerated. There could be contributions from other charge states because current plasma torus models consist mostly of ions with low charge states, consistent with photoionization and ion-neutral charge exchange in a low-density plasma and neutral gas environment. The 250–1000 eV energy flux at the telescope aperture was $2.4 \times 10^{-14} \text{ erg cm}^{-2} \text{ s}^{-1}$, corresponding to a luminosity of 0.12 GW. Although bremsstrahlung from nonthermal electrons might account for a significant fraction of the continuum X-rays, the physical origin of the observed IPT X-ray emission is not yet fully understood. The 2003 jovian *Chandra* observations also detected X-ray emission from the IPT, although at a fainter level than in 1999 or 2000. The morphology exhibited the familiar dawn-to-dusk asymmetry.

9. Saturn

The production of X-rays at Saturn was expected because, like the Earth and Jupiter, Saturn was known to possess a magnetosphere and energetic electrons and ions particles within it; however, early attempts to detect X-ray emission from Saturn with *Einstein* in December 1979 and with *ROSAT* in April 1992 were negative and marginal, respectively. Saturnian X-rays were unambiguously observed by *XMM-Newton* in October 2002 and by the *Chandra* X-ray Observatory in April 2003. In January 2004, Saturn was again observed by the *Chandra* ACIS-S in two exposures, one on 20 January and other on 26–27 January, with each observation lasting for about one full Saturn rotation. The X-ray power emitted from Saturn’s disk is roughly one-fourth of that from Jupiter’s disk, which is consistent with Saturn being twice as far as Jupiter from Sun and Earth.

The January 2004 *Chandra* observation showed (Fig. 11) that X-rays from Saturn are highly variable—a factor of 2 to 4 variability in brightness over 1 week. These observations also revealed X-rays from Saturn’s south polar cap on January 20 (see Fig. 11, left panel), which are not evident in the January 26 observation (see Fig. 11, right panel) and in earlier *Chandra* observations. X-rays from the south polar cap region were present only in the 0.7–1.4 keV energy band, in contrast with Jupiter’s X-ray aurora for which the

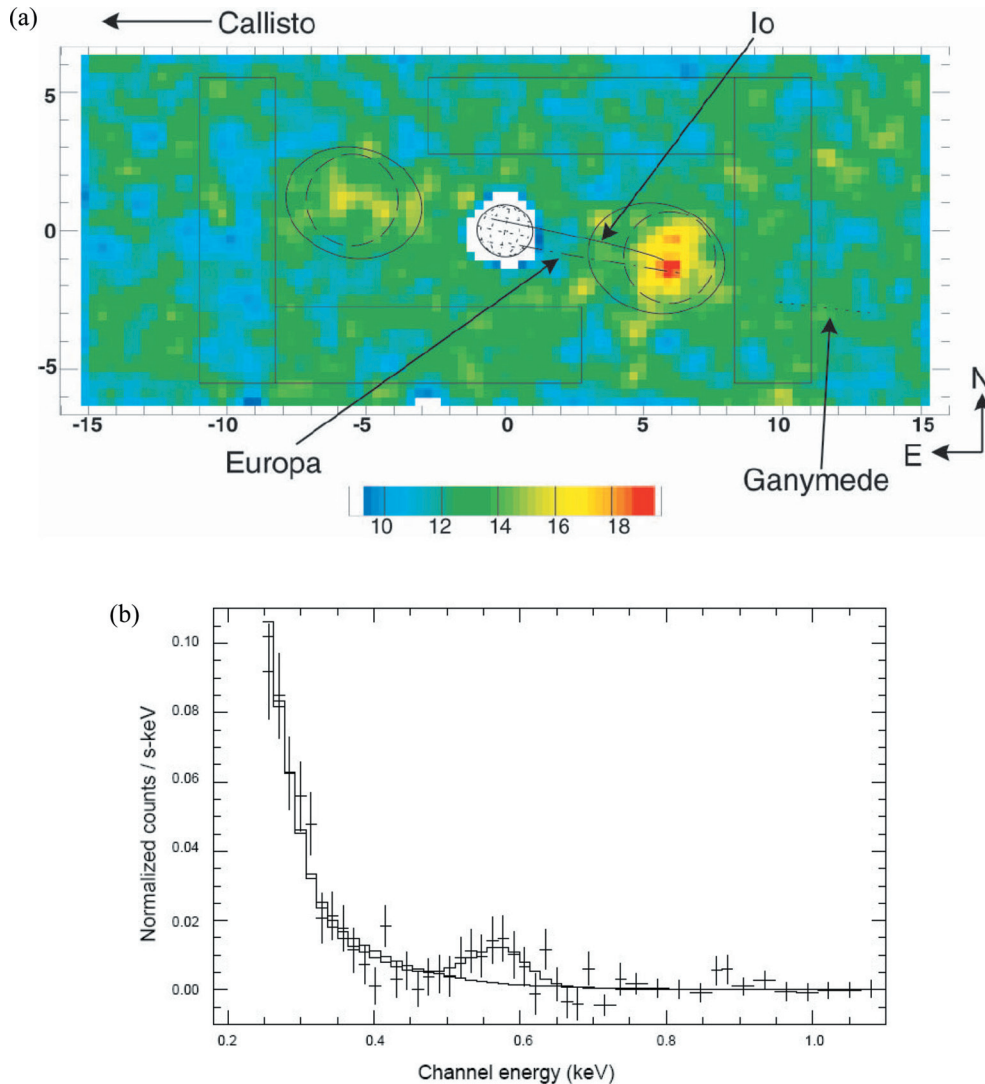


FIGURE 10 Plasma Torus. (a) Chandra/HRC-I image of the IPT (2000 December 18). The image has been smoothed by a two-dimensional Gaussian with $\sigma = 7.38''$ (56 HRC-I pixels). The axes are labeled in units of Jupiter's radius, R_J , and the scale bar is in units of smoothed counts per image pixel. The paths traces by Io, Europa, and Ganymede are marked on the image. Callisto is off the image to the dawn side, although the satellite did fall within the full microchannel plate field of view. The regions bounded by rectangles were used to determine background. The regions bounded by dashed circles or solid ellipses were defined as source regions. (b) Chandra/ACIS-S spectrum for the Io Plasma Torus from November 1999. The solid line presents a model fit for the sum of a power-law spectrum and a Gaussian line, while the dashed line represents just a pure power law spectrum. The line is consistent with K-shell fluorescent emission from oxygen ions. [From Elsner et al., *Astrophysical Journal*, 572, 1077–1082, 2002].]

emission is mostly in the bands 0.3–0.4 keV and 0.6–0.7 keV. Because of this, it is likely that the X-ray emission from the south polar cap is unlikely to be auroral in nature, and more likely that they are an extension of the disk X-ray emission of Saturn. Any emission from the north polar cap region was blocked by Saturn's rings.

As is the case for Jupiter's disk, X-ray emission from Saturn seems likely to be due to the scattering of the incident solar X-ray flux. An X-ray flare has been detected from the nonauroral disk of Saturn during the *Chandra* observation on 20 January 2004. Taking light travel time into account, this X-ray flare from Saturn coincided with an M6-class flare emanating from a sunspot that was clearly visible from both Saturn and Earth. Moreover, the lightcurve for the X-rays from Saturn was very similar to that of the solar X-ray flux. This was the first direct evidence suggesting that Saturn's disk X-ray emission is principally controlled by processes happening on the Sun. Further, a good correla-

tion has been observed between Saturn X-rays and F10.7 solar activity index: suggesting a solar connection.

The spectrum of X-rays from Saturn's disk is very similar to that from Jupiter's disk. Saturn's disk spectrum measured on 20 January 2004 is quite similar to that measured on 14–15 April 2003 in the 0.3–0.6 keV range. However, at energies 0.6–1.2 keV, the former is stronger by a factor of 2 to 4. This is probably due to the nature of the M6-class solar X-ray flare on 20 January, with a corresponding hardening of the solar X-ray flux driving Saturn's X-ray emission.

10. Rings of Saturn

The rings of Saturn, known to be made of mostly water (H_2O) ice, are one of the most fascinating objects in our solar system. Recently, the discovery of X-rays from the rings

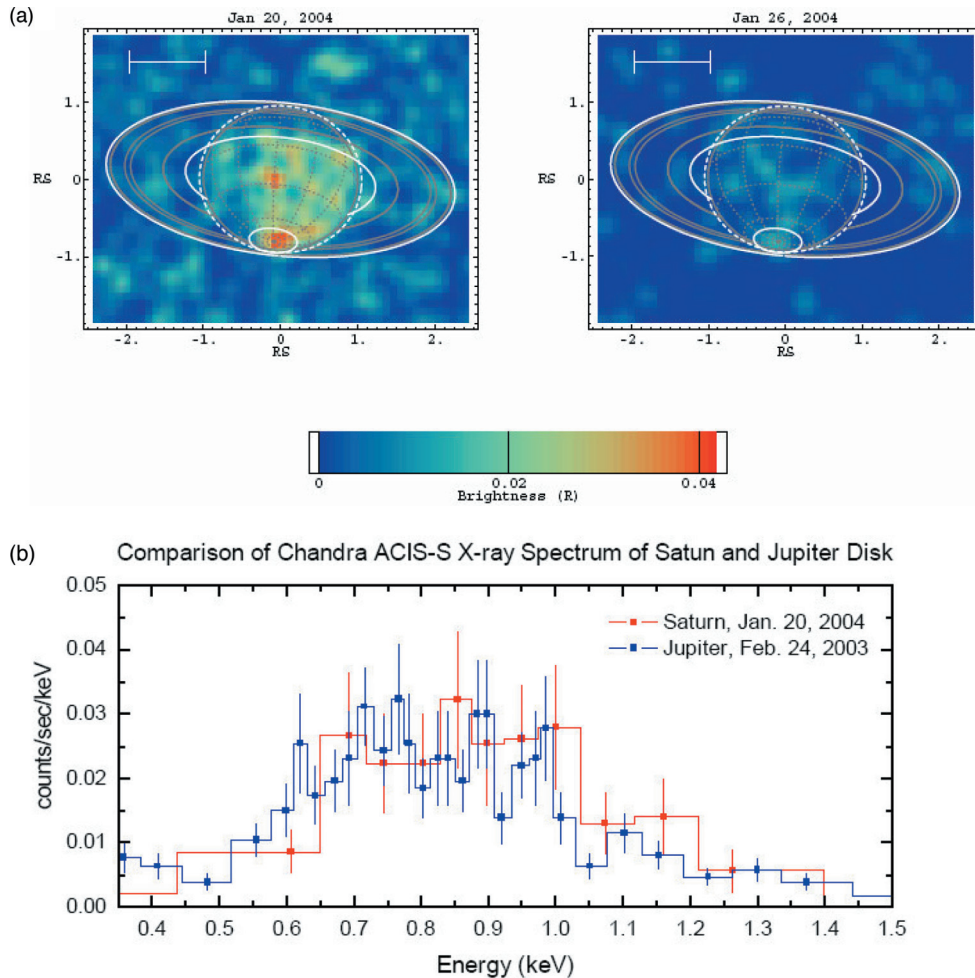


FIGURE 11 Saturn. (a) Chandra ACIS X-ray 0.24–2.0 keV images of Saturn on January 20 and 26, 2004. Each continuous observation lasted for about one full Saturn rotation. The horizontal and vertical axes are in units of Saturn’s equatorial radius. The white scale bar in the upper left of each panel represents 10^2 . The two images, taken a week apart and shown on the same color scale, indicate substantial variability in Saturn’s X-ray emission. [from Bhardwaj et al. *Astrophysical Journal Letters*, 624, L121–L124 2005]. (b) Disk X-ray spectrum of Saturn (red curve) and Jupiter (blue curve). Values for Saturn spectrum are plotted after multiplying by a factor of 5. [from Bhardwaj, *Advances in Geosciences*, vol.3, 215–230, 2006].

of Saturn was made from the *Chandra* ACIS-S observations of the Saturnian system conducted in January 2004 and April 2003. X-rays from the rings are dominated by emission in a narrow (~ 130 eV wide) energy band of 0.49–0.62 keV (Fig. 12). This band is centered on the oxygen $K\alpha$ fluorescence line at 0.53 keV, suggesting that fluorescent scattering of solar X-rays from oxygen atoms in the surface of H_2O icy ring material is the likely source mechanism for ring X-rays. The X-ray power emitted by the rings in the 0.49–0.62 keV band on 20 January 2004 is 84 MW, which is about one-third of that emitted from the Saturn disk in the 0.24- to 2.0-keV band. The projected rings have about half the surface area of the Saturn disk, consistent with this ratio. During 14–15 April 2003, the X-ray power emitted by the rings in the 0.49- to 0.62-keV band is about 70 MW.

Figure 12 shows the X-ray image of the Saturnian system in January 2004 in the 0.49- to 0.62-keV band, the energy range where X-rays from the rings are unambiguously detected. The observations of January 2004 also suggested that, similar to Saturn’s X-ray emission, the ring X-rays are highly variable—a factor of 2–3 variability in brightness over

1 week. There is an apparent asymmetry in X-ray emission from the east (morning) and west (evening) ansae of the rings (see Fig. 12a). However, when the *Chandra* ACIS-S data set of January 2004 and April 2003 is combined, the evidence for asymmetry is not that strong.

11. Comets

The discovery of high-energy X-ray emission in 1996 from C/1996 B2 (Hyakutake) created a new class of X-ray-emitting objects. Observations since 1996 have shown that the very soft ($E < 1$ keV) emission is due to an interaction between the solar wind and the comet’s atmosphere, and that X-ray emission is a fundamental property of comets. Theoretical and observational work has demonstrated that charge exchange collision of highly charged heavy solar wind ions with cometary neutral species is the best explanation for the emission. The X-rays are extremely easy to detect because the neutral atmosphere of a comet is large and extended and gravitationally unbound, intercepting a

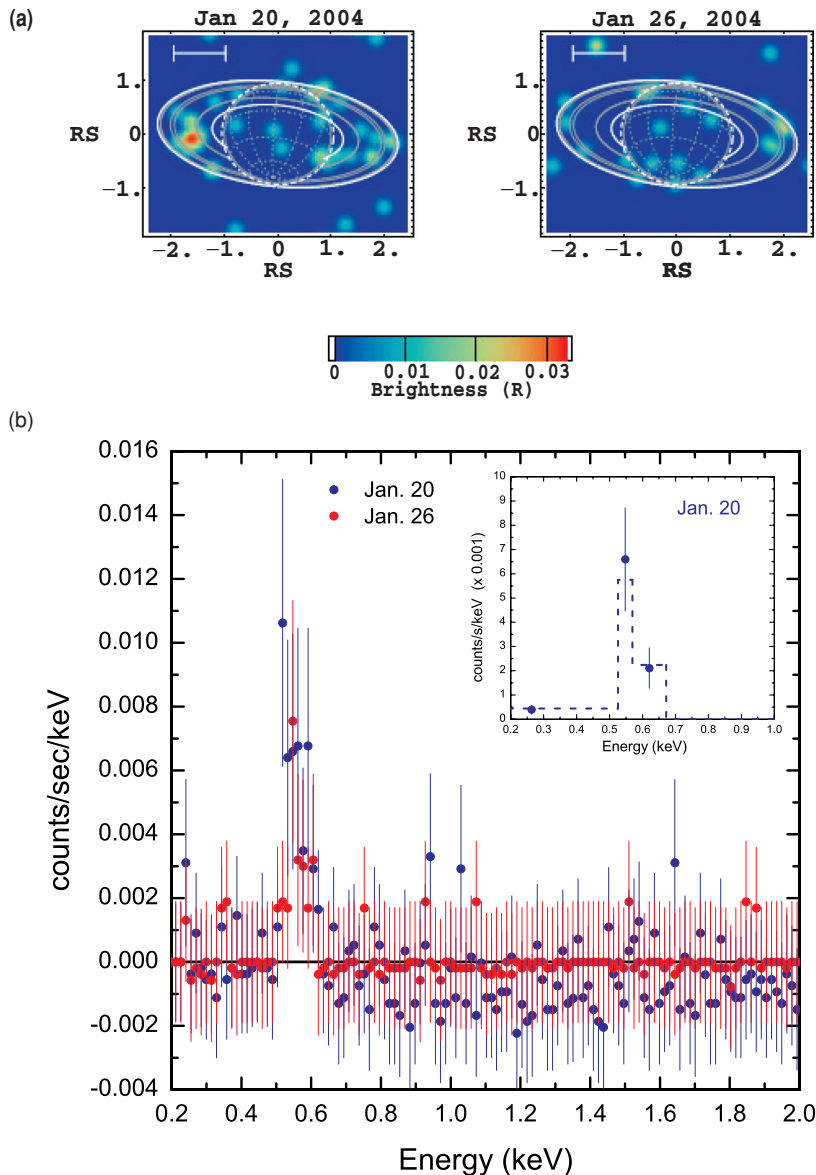


FIGURE 12 Saturn's Rings. (a) Chandra ACIS X-ray images of the Saturnian system in the 0.49–0.62 keV band on 2004 January 20 and 26–27. The X-ray emission from the rings is clearly present in these restricted energy band images; the emission from the planet is relatively weak in this band (see Fig. 11(a) for an X-ray image of the Saturnian system in the 0.24–2.0 keV band). (b) Background-subtracted Chandra ACIS-S3-observed X-ray energy spectrum for Saturn's rings in the 0.2–2.0 keV range on 2004 January 20 and 26–27. The cluster of X-ray photons in the ~ 0.49 –0.62 keV band suggests the presence of the oxygen $K\alpha$ line emission at 0.53 keV in the X-ray emission from the rings. The inset shows a Gaussian fit (peak energy = 0.55 keV, $\sigma = 140$ eV), shown by the dashed line, to the ACIS-observed rings' spectrum on January 20. Each spectral point (filled circle with error bar) represents ≥ 10 measured events. The spectral fitting suggests that X-ray emissions from the rings are predominantly oxygen $K\alpha$ photons. [from Bhardwaj et al., *Astrophys. J. Lett.*, 627, L73-L76, 2005].

large amount of solar wind ions as they stream away from the Sun. The observed characteristics of the emission can be organized into the following four categories: (1) spatial morphology, (2) total X-ray luminosity, (3) temporal variation, and (4) energy spectrum. Any physical mechanism that purports to explain cometary X-ray emission must account for all of these characteristics.

X-Ray and EUV images of C/1996 B2 (Hyakutake) made by the *ROSAT* and *EUVE* satellites look very similar (Fig. 13). Except for images of C/1990 N1 and C/Hale-Bopp 1995 O1, all EUV and X-ray images of comets have exhibited similar spatial morphologies. The emission is largely confined to the sunward side of the cometary coma; almost no emission is found in the extended tails of dust or

plasma. The peak X-ray brightness gradually decreases with increasing cometocentric distance r with a dependence of about r^{-1} . The brightness merges with the soft X-ray background emission at distances that exceed 10^4 km for weakly active comets, and can exceed 10^6 km for the most luminous comets. The region of peak emission is crescent-shaped with a brightness peak displaced towards the Sun from the nucleus. The distance of this peak from the nucleus appears to increase with increasing values of Q (total gas production rate); for Hyakutake, it was located at $r_{\text{peak}} \sim 2 \times 10^4$ km.

The observed X-ray luminosity, L_x , of C/1996 B2 (Hyakutake) was 4×10^{15} ergs s^{-1} for an aperture radius at the comet of 1.2×10^5 km. (Note that the photometric luminosity depends on the energy bandpass and the observational

aperture at the comet. The quoted value assumes a *ROSAT* photon emission rate of $P_X \sim 10^{25} \text{ s}^{-1}$ (0.1–0.6 keV), in comparison to the *EUVE* estimate of $P_{\text{EUV}} \sim 7.5 \times 10^{25} \text{ s}^{-1}$ (0.07–0.18 keV and 120,000-km aperture). A positive correlation between optical and X-ray luminosities was demonstrated using observations of several comets having similar gas ($Q_{\text{H}_2\text{O}}$)-to-dust ($Af\rho$) emission rate ratios. L_x correlates more strongly with the gas production rate Q_{gas} than it does with $L_{\text{opt}} \sim Q_{\text{dust}} \sim Af\rho$. Particularly dusty comets, like Hale–Bopp, appear to have less X-ray emission than would be expected from their overall optical luminosity L_{opt} . The peak X-ray surface brightness decreases with increasing heliocentric distance r , independent of Q , although the total luminosity appears roughly independent of r . The maximum soft X-ray luminosity observed for a comet to date is $\sim 2 \times 10^{16} \text{ erg s}^{-1}$ for C/Levy at 0.2–0.5 keV.

Photometric lightcurves of the X-ray and EUV emission typically show a long-term baseline level with superimposed impulsive spikes of a few hours' duration, and maximum amplitude 3 to 4 times that of the baseline emission level. Figure 13 demonstrates the strong correlation found between the time histories of the solar wind proton flux (a proxy for the solar wind minor ion flux), the solar wind magnetic field intensity, and a comet's X-ray emission, for the case of comet 2P/Encke 19997. Comparison of the *ROSAT* and *EUVE* luminosity of C/1996 B2 (Hyakutake) with time histories of the solar wind proton flux, oxygen ion flux, and solar X-ray flux, showed a strongest correlation between the cometary emission and the solar wind oxygen ion flux, a good correlation between the comet's emission and the solar wind proton flux, but no correlation between the cometary emission and the solar X-ray flux.

Until 2001, all published cometary X-ray spectra had very low spectral energy resolution ($\Delta E/E \sim 1$ at 300–600 eV), and the best spectra were those obtained by *ROSAT* for C/1990 K1 (Levy) and by *BeppoSAX* for comet C/1995 O1 (Hale–Bopp). These observations were capable of showing that the spectrum was very soft (characteristic thermal bremsstrahlung temperature $kT \sim 0.23 \pm 0.04 \text{ keV}$) with intensity increasing toward lower energy in the 0.01- to 0.60-keV energy range and established upper limits to the contribution of the flux from K-shell resonance fluorescence of carbon at 0.28 keV and oxygen at 0.53 keV. However, even in these “best” spectra, continuum emission (such as that produced by the thermal bremsstrahlung mechanism) could not be distinguished from a multiline spectrum, such as would result from the SWCX mechanism. Nondetections of comets C/Hyakutake, C/Tabur, C/Hale–Bopp, and 55P/Tempel–Tuttle using the XTE PCA (2–30 keV) and ASCA SIS (0.6–4 keV) imaging spectrometers were consistent with an extremely soft spectrum.

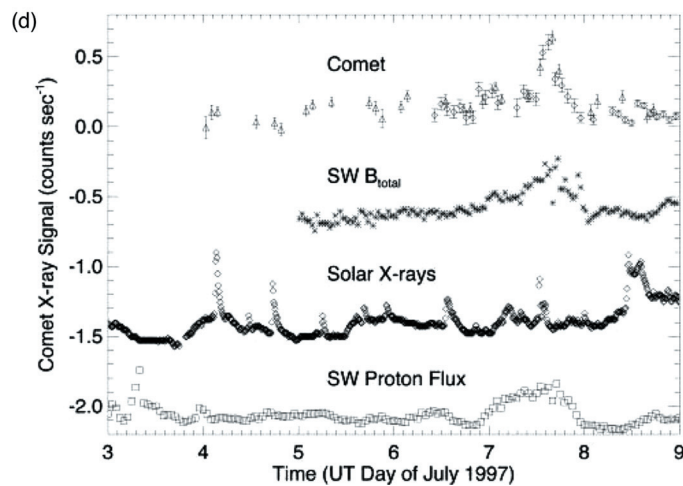
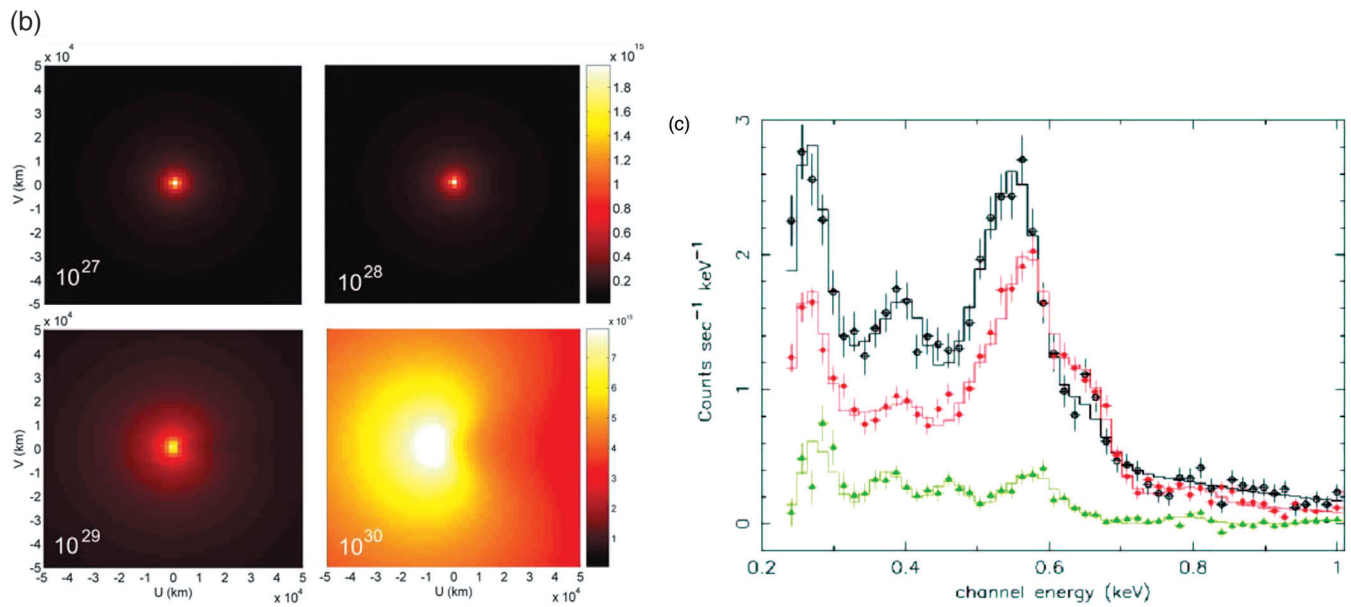
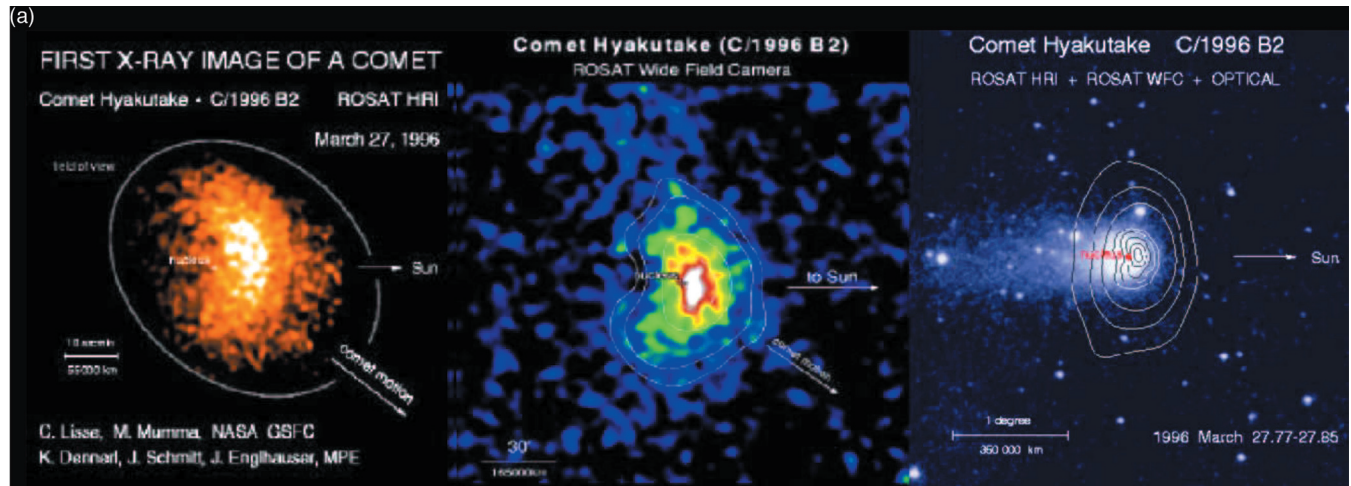
Higher resolution spectra of cometary X-ray emission have now appeared in the literature. The *Chandra* X-ray Observatory (CXO) measured soft X-ray spectra

from comet C/1999 S4 (LINEAR) over an energy range of 0.2–0.8 keV, and with a full width half maximum energy resolution of $\Delta E = 0.11 \text{ keV}$ (Fig. 13). The spectrum is dominated by line emission from C^{+4} , C^{+5} , O^{+6} , and O^{+7} excited ions, not by continuum. A spectrum of comet C/1999 T1 (McNaught–Hartley) showed similar line emission features, with a somewhat higher ratio of OVII to OVIII emission, and emission due to Ne^{+9} . A new spectrum of comet 2P/Encke shows a very different ratio of line emission in the C^{+4} , C^{+5} , O^{+6} , and O^{+7} lines, due to the collisionally thin nature of the low activity coma, and the unusual postshock charge state of the solar wind at the time of observation. Line emission is also found in *XMM-Newton* spectra of comet C/1999 T1 (McNaught–Hartley) and, more recently, in CXO spectra of C/2001 WM1 (Lincoln Near-East Asteroid Research, Linear) and C/2002 Ikeya–Zhang. An *XMM-Newton* spectrum of C/2001 WM1 (LINEAR) shows characteristic SWCX X-ray signatures in unprecedented detail.

From other work, there are suggestions of charge exchange line emission from other species than $\text{C}^{+4}/\text{C}^{+5}$, $\text{O}^{+6}/\text{O}^{+7}$, and Ne^{+9} . A reanalysis of archival *EUVE* Deep Survey spectrometer spectra suggests EUV line emission features from comet C/1996 B2 (Hyakutake) due to O^{+} , O^{+5} , O^{+4} , C^{+4} , O^{+6} , C^{+5} , He^{+} , and Ne^{+7} . It has been suggested that emission lines are attributable to Mg and Si in C/McNaught–Hartley, and He^{+2} in C/Hale–Bopp, although these remain unconfirmed and controversial due to the sensitivity of the results on the details of the instrumental background subtraction. Hints of possible emission due to N^{+6} at 425 eV contributing to a reduced 380/450 eV ratio were found in *Chandra* observations of 2P/Encke in 2003.

Numerical simulations of the solar wind interaction with Hyakutake including SWCX have been used to generate X-ray images. A global magneto-hydrodynamic (MHD) model and a hydrodynamic model were used to predict solar wind speeds and densities in addition to the X-ray emission around a comet. The simulated X-ray images are similar to the observed images. Recent work has shown that by determining the location of the emission maximum in the collisionally thick case, the neutral gas production rate can be determined in 5 comets observed by *ROSAT* and *XMM-Newton*. On comet WM1, the position of the cometary bow shock has been determined using the location of rapid changes in the first and second derivatives of the flux with distance from the nucleus.

It is not clear that the emission pattern always follows the plasma structures. New work suggests that the crescent-shaped, sunward offset morphology is found only for comets with coma dense enough to be in the collisionally thick regime—for low activity comets, the emission will be maximal wherever the coma has its maximum density, typically at the nucleus. This may explain the unusual emission



morphologies seen in comets like d'Arrest 1997 and 2P/Encke 2003.

Up until now, the temporal variation of the solar wind dominated the observed behavior on all but the longest timescales of weeks to months. A “new” form of temporal variation has recently been demonstrated in the *Chandra* observations of comet 2P/Encke 2003, wherein the observed X-ray emission is modulated at the 11.1-hour period of the nucleus rotation. Rotational modulation of the signal should be possible only in collisionally thin (to SWCX) comae with weak cometary activity, where a change in the coma neutral gas density can directly affect power density of cometary X-ray.

Driven by the solar wind, cometary X-rays provide an observable link between the solar corona, where the solar wind originates, and the solar wind where the comet resides. Once we have understood the SWCX mechanism's behavior in cometary comae in sufficient detail, we will be able to use comets as probes to measure the solar wind throughout the heliosphere. This will be especially useful in monitoring the solar wind in places hard to reach with spacecraft—such as over the solar poles, at large distances above and below the ecliptic plane, and at heliocentric distances greater than a few AU. For example, about one-third of the observed soft X-ray emission is found in the 530- to 700-eV oxygen O^{+7} and O^{+6} lines; observing photons of this energy will allow studies of the oxygen ion charge ratio of the solar wind, which is predicted to vary significantly between the slow and fast solar winds at low and high solar latitudes, respectively.

12. Asteroids

X-Rays from asteroids have been studied by experiments on two *in situ* missions, the X-ray/gamma-ray spectrometer (XGRS) on the Near Earth Asteroid Rendezvous (NEAR)–Shoemaker mission to asteroid 433 Eros, and the X-ray spectrometer (XRS) on the *Hayabusa* mission to asteroid 25143 Itokawa. The only attempt to detect X-rays from an asteroid was a 10-ks distant, remote observation by *Chandra* on 11 December 2001 of 1998 WT24, but it was unsuccessful. The results of the *in situ* observations show X-ray emission due to fluorescence and scattering of incident solar X-rays, similar to the emission seen from the surface of the airless Moon. In fact, the best measurements were obtained during a strong solar flare, when the incident solar X-rays were highly amplified. As for the Moon, X-ray spectroscopy of resonantly scattered solar X-rays can be used to map the elemental composition of the surface.

NEAR–Shoemaker entered Eros orbit on 14 February 2000 and completed a 1-year long mission around it. Eros at $33 \times 13 \times 13$ km in size is the second largest near-Earth asteroid, and its “day” is 5.27 hours long. Eros exhibits a heavily cratered surface with one side dominated by a huge, scallop-rimmed gouge; a conspicuous sharp, raised rimmed crater occupies the other side. The XRS part of the XGRS detected X-rays in the 1- to 10-keV energy range to determine the major elemental composition of Eros' surface. The XRS observed the asteroid in low orbit (<50 km) during 2 May–12 August 2000 and again during 12 December 2000–2 February 2001. These observations suggest that

FIGURE 13 The Rich Behavior of X-Ray Emission Seen From Comets. (a) Cometary X-ray Emission Morphology. Images of C/Hyakutake 1996B2 on 26 - 28 March 1996 UT: ROSAT HRI 0.1 - 2.0 keV X-ray, ROSAT WFC .09 - 0.2 keV extreme ultraviolet, and visible light, showing a coma and tail, with the X-ray emission contours superimposed. The Sun is towards the right, the plus signs mark the position of the nucleus, and the orbital motion of the comet is towards the lower right in each image. [From Lisse et al., *Science* 292, 1343 - 1348, 1996]. (b) Morphology as a function of comet gas production rate (given in terms of molecules sec^{-1} in the lower right of each panel). Note the decreasing concentration of model source function and the increasing importance of diffuse halo emission in the extended coma as the gas production rate increases. [from Lisse et al., *Astrophys. J.*, **635**, 1329-1347, 2005]. (c) *Chandra* ACIS medium resolution CCD X-ray spectra of the X-ray emission from three comets. All curves show ACIS-S3 measurements of the 0.2 - 1.5 keV pulse height spectrum, as measured in direct detection mode. with ± 1 error bars and the best-fit emission line + thermal bremsstrahlung model convolved with the ACIS-S instrument response as a histogram. The positions of several possible atomic lines are noted. Pronounced emission due to O^{7+} and O^{6+} is evident at 560 and 660 eV, and for C^{5+} , C^{4+} , and N^{5+} emission lines at 200 - 500 eV. Best-fit model lines at 284, 380, 466, 552, 590, 648, 796, and 985 are close to those predicted for charge exchange between solar wind C^{+5} , C^{+6} , C^{+6}/N^{+6} , O^{+7} , O^{+7} , O^{+8} , O^{+8} , and Ne^{+9} ions and neutral gases in the comet's coma. (Black) ACIS spectra of C/LINEAR 1999 S4 (circles), from Lisse et al. (2001). (Red) Comet McNaught-Hartley spectra (squares), after Krasnopolsky et al. 2003. (Green) 2P/Encke spectrum taken on 24 Nov 2003, multiplied by a factor of 2. The C/1999 S4 (LINEAR) and C/McNaught-Hartley 2001 observations had an average count rate on the order 20 times as large, even though Encke was closer to *Chandra* and the Earth when the observations were being made. Note the 560 complex to 400 eV complex ratio of 2 to 3 in the two bright, highly active comets, and the ratio of approximately 1 for the faint, low activity comet Encke. [from Lisse et al., op. cit 2005]. (d) Temporal trends of the cometary X-ray emission. Lightcurve, solar wind magnetic field strength, solar wind proton flux, and solar X-ray emission for 2P/Encke 1997 on 4-9 July 1997 UT. All error bars are ± 1 . D - HRI light curve, 4-8 July 1997. \diamond - EUVE scanner Lexan B light curve 6 - 8 July 1997 UT, taken contemporaneously with the HRI observations, and scaled by a factor of 1.2. Also plotted are the WIND total magnetic field B_{total} ($^{\circ}$), the SOHO CELIAS/SEM 1.0 - 500 Å solar X-ray flux (\diamond), and the SOHO CELIAS solar wind proton flux (boxes). There is a strong correlation between the solar wind magnetic field/density and the comet's emission. There is no direct correlation between outbursts of solar X-rays and the comet's outbursts. [from Lisse et al., *Icarus* **141**, 316-330, 1997].

elemental ratios for Mg/Si, Al/Si, Ca/Si, and Fe/Si on Eros are most consistent with a primitive chondrite and give no evidence of global differentiation. The S/Si ratio is considerably lower than that for a chondrite and is most likely due to surface volatilization (“space weathering”). The overall conclusion is that Eros is broadly “primitive” in its chemical composition and has not experienced global differentiation into a core, mantle, and crust, and that surface effects cause the observed departures from chondritic S/Si and Fe/Si.

Hayabusa reached the asteroid 25143 Itokawa on 12 September 2005. The first touchdown occurred on 19 November 2005. The observations made during the touchdown, a period of relatively enhanced solar X-ray flux, returned an average elemental mass ratio of Mg/Si = 0.78 ± 0.07 and Al/Si = 0.07 ± 0.03 . These early results suggest that, like Eros, asteroid Itokawa’s composition can be described as an ordinary chondrite, although occurrence of some differentiation cannot be ruled out.

The composition and structure of the rocks and minerals in asteroids provides critical clues to their origin and evolution and are a fundamental line of inquiry in understanding the asteroids, of which more than 20,000 have been de-

tected and catalogued. It is interesting to note that for both Eros and Itokawa the compositions derived by remote X-ray observations using spacecraft in close proximity to the asteroid seem consistent with those found using Earth-based optical and infrared spectroscopy.

13. Heliosphere

The solar wind flow starts out slowly in the corona but becomes supersonic at a distance of few solar radii. The gas cools as it expands, falling from $\sim 10^6$ K down to about 10^5 K at 1 AU. The average properties of the solar wind at 1 AU are proton number density $\sim 7 \text{ cm}^{-3}$, speed $\sim 450 \text{ km s}^{-1}$, temperature $\sim 10^5$ K, magnetic field strength ~ 5 nT, and Mach number ~ 8 . However, the composition and charge state distribution far from the Sun are “frozen-in” at coronal values due to the low collision frequency outside the corona. The solar wind contains structure, such as slow (400 km s^{-1}) and fast (700 km s^{-1}) streams, which can be mapped back to the Sun. The solar wind “terminates” in a shock called the heliopause, where the ram pressure of the streaming

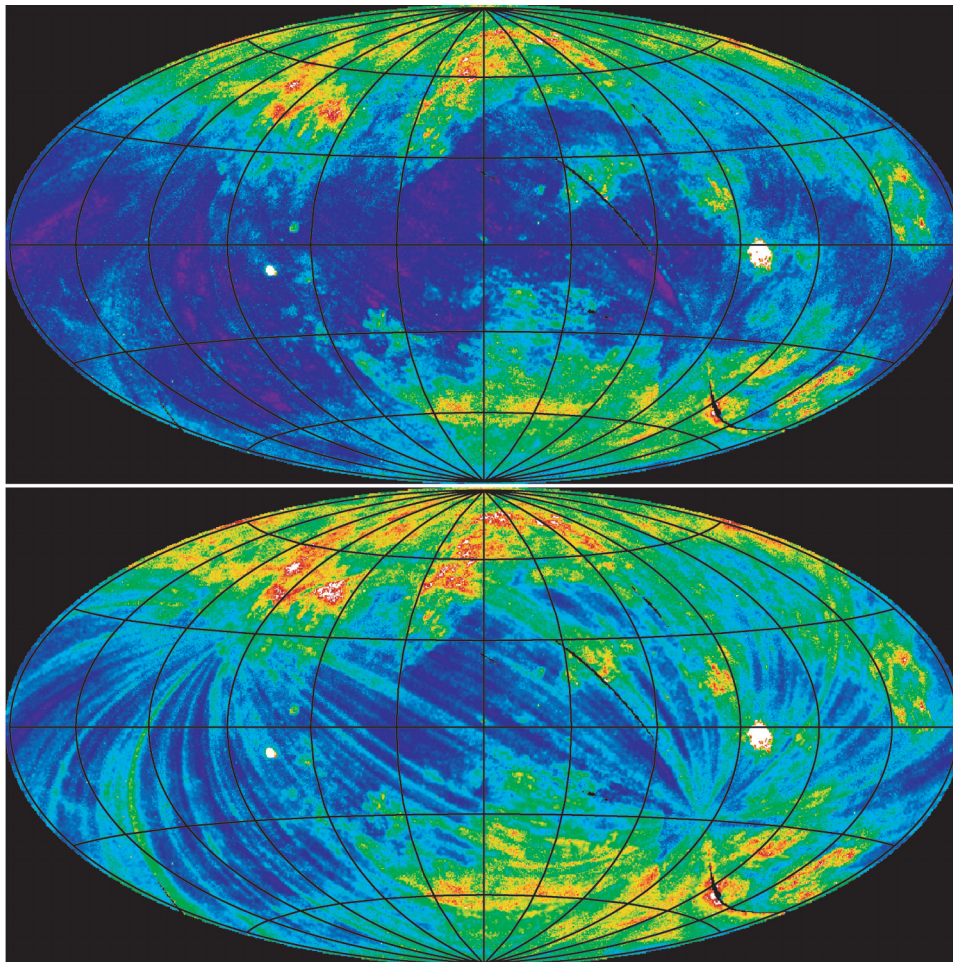


FIGURE 14 Heliosphere. Upper panel) ROSAT All-Sky Survey map of the cosmic X-ray background at 1/4 keV. The data are displayed using an Aitoff projection in Galactic coordinates centered on the Galactic center with longitude increasing to the left and latitude increasing upwards. Low intensity is indicated by purple and blue while red indicates higher intensity. Lower panel) Same as above except the contaminating long-term enhancements (SWCX emission) were not removed. The striping is due to the survey geometry where great circles on the sky including the ecliptic poles were scanned precessing at $\sim 1^\circ$ per day. [from Snowden et al., *Astrophys. J.*, **485**, 125–135 1997].

TABLE 1 Summary of the Characteristics of Soft X-Ray Emission from Solar System Bodies

Object	Emitting Region	Power Emitted ^a	Special Characteristics	Possible Production Mechanism
Earth	Auroral atmosphere	10–30 MW	Correlated with magnetic storm and substorm activity	Bremsstrahlung from precipitating electrons + characteristic line emission from atmospheric neutrals due to electron impact
Earth	Nonauroral atmosphere	40 MW	Correlated with solar X-ray flux	Scattering of solar X-rays by atmosphere
Jupiter	Auroral atmosphere	0.4–1 GW	Pulsating (~20–60 min) X-ray hot spot in north polar region	Energetic ion precipitation from magnetosphere and/or solar wind + electron bremsstrahlung
Jupiter	Nonauroral atmosphere	0.5–2 GW	Relatively uniform over disk	Resonant scattering of solar X-rays + possible ion precipitation from radiation belts
Moon	Dayside surface	0.07 MW	Correlated with solar X-rays	Scattering and fluorescence due to solar X-rays by the surface elements on dayside.
	Night side (geocoronal)		Night side emissions are ~1% of the day side	SWCX with geocorona
Comets	Sunward-side coma	0.2–1 GW	Intensity peaks in sunward direction, ~10 ⁵ –10 ⁶ km ahead of cometary nucleus, and is correlated with solar wind parameters	SWCX with cometary neutrals
Venus	Sunlit atmosphere	50 MW	Emissions from ~120 to 140 km above the surface	Fluorescent scattering of solar X-rays by C and O atoms in the atmosphere
Mars	Sunlit atmosphere	1–4 MW	Emissions from upper atmosphere at heights of 110–130 km	Fluorescent scattering of solar X-rays by C and O atoms in the upper atmosphere
	Exosphere	1–10 MW	Emissions extend out to ~8 Mars radii	SWCX with Martian corona
Io	Surface	2 MW	Emissions from upper few micrometers of the surface	Energetic jovian magnetospheric ions impact on the surface
Europa	Surface	3 MW	Emissions from upper few micrometers of the surface	Energetic jovian magnetospheric ions impact on the surface
Io plasma torus	Plasma torus	0.1 GW	Dawn-dusk asymmetry observed	Electron bremsstrahlung + ?
Saturn	Sunlit disk	0.1–0.4 GW	Varies with solar X-rays	Scattering of solar X-rays + Electron bremsstrahlung ?
Rings of Saturn	Surface	80 MW	Emissions confined to a narrow energy band around at 0.53 keV.	Fluorescent scattering of solar X-rays by atomic oxygen in H ₂ O ice + ?
Asteroid	Sunlit surface		Emissions vary with solar X-ray flux	Fluorescent scattering of solar X-rays by elements on the surface
Heliosphere	Entire heliosphere	10 ¹⁶ W	Emissions vary with solar wind	SWCX with heliospheric neutrals

^a The values quoted are values at the time of observation. X-rays from all bodies are expected to vary with time. For comparison, the total X-ray luminosity from the Sun is 10²⁰ W. SWCX ≡ solar wind charge exchange = charge exchange of heavy, highly ionized solar wind ions with neutrals.

solar wind has fallen to that of the ISM gas. The region of space containing plasma of solar origin, from the corona to the heliopause at ~ 100 AU, is called the heliosphere. A very small part of the solar wind interacts with the planets and comets; the bulk of the wind interacts with neutral ISM gas in the heliosphere and neutral and ionized interstellar medium (ISM) at the heliopause.

X-Ray emission from the heliosphere has also been predicted from the interaction of the solar wind with the interstellar neutral gas (mainly HI and HeI) that streams into the solar system. It has been demonstrated that roughly half of the observed 0.25-keV X-ray diffuse background can be attributed to this process (see Fig. 14). SoHO observations of neutral hydrogen Lyman alpha emission show a clear asymmetry in the ISM flow direction, with a clear deficit of neutral hydrogen in the downstream direction of the incoming neutral ISM gas, most likely created by SWCX ionization of the ISM. The analogous process applied to other stars has been suggested as a means of detecting stellar winds. Also a strong correlation between the solar wind flux density and the *ROSAT* “long-term enhancements,” systematic variations in the soft X-ray background of the *ROSAT* X-ray detectors has been shown. Photometric imaging observations of the lunar night side by *Chandra* made in September 2001 do not show any lunar night side emission above a SWCX background. The soft X-ray emission detected from the dark side of the Moon, using *ROSAT*, would appear to be attributable not to electrons spiraling from the sunward to the dark hemisphere, as proposed earlier, to SWCX in the column of heliosphere between the Earth and the Moon.

Just as charge exchange–driven X-rays are emitted throughout the heliosphere, similar emission must occur within the astrospheres of other stars with highly ionized stellar winds that are located within interstellar gas clouds that are at least partially neutral. Although very weak, in principle, this emission offers the opportunity to measure mass-loss rates and directly image the winds and astrospheres of other main sequence late-type stars. Imaging would provide information on the geometry of the stellar wind, such as whether outflows are primarily polar, azimuthal, or isotropic, and whether or not other stars have analogs of the slow (more ionized) and fast (less ionized) solar wind streams.

14. Summary

Table 1 summarizes our current knowledge of the X-ray emissions from the planetary bodies that have been ob-

served to produce soft X-rays. Several other solar system bodies, including Titan, Uranus, Neptune, and inner-icy satellites of Saturn, are also expected to be X-ray sources, but they are yet to be detected. During its flyby in 2008–2009, NASA’s *MESSENGER* spacecraft will measure X-rays from Mercury by the onboard XRS experiment. Such measurements will continue after insertion of *MESSENGER* in the Herminian orbit in 2011. The *MESSENGER* XRS will provide information on elemental composition in the Mercury surface by observing the $K\alpha$ line of elements present that are induced by solar X-rays as well as by high-energy electron precipitation.

Acknowledgments

A large part of this chapter is based on the review article by Bhardwaj et al. (2006), which is a collective effort of several authors, and we deeply acknowledge all the authors of that paper. We also thank the entire solar system X-ray community whose work have led to this review.

Bibliography

- Bhardwaj, A. (2006). X-Ray emission from Jupiter, Saturn, and Earth: A short review. In “Advances in Geosciences,” vol. 3, pp. 215–230. World Scientific, Singapore.
- Bhardwaj, A., Elsner, R. F., Gladstone, G. R., Cravens, T. E., Lisse, C. M., Dennerl, K., Branduardi-Raymont, G., Bradford, J., Wargelin, J., Hunter Waite, Jr., J., Robertson, I., Ostgaard, N., Beiersdorfer, P., Snowden, S. L., and Kharchenko, V. (2006). X-Rays from solar system bodies. *Planetary and Space Science*, in press.
- Dennerl, K., Lisse, C. M., Bhardwaj, A., Burwitz, V., Englhauser, J., Gunnels, H., Holmström, M., Jansen, F., Kharchenko, V., and Rodríguez-Pascual, P. M. (2006). First observation of Mars with *XMM-Newton*. High resolution X-ray spectroscopy with RGS. *Astronomy and Astrophysics* **451** (2), 709–722.
- Dennerl, K., Burwitz, V., Englhauser, J., Lisse, C., and Wolk, S. (2002). Discovery of X-rays from Venus with *Chandra*. *Astronomy and Astrophysics* **386**, 319–330; A&A homepage.
- Krasnopolsky, V. A., Greenwood, J. B., and Stancil, P. C. (2004). X-Ray and extreme ultraviolet emission from comets. *Space Science Review* **113**, 271–374.
- Lisse, C. M., Cravens, T. E., and Dennerl, K. (2004). X-Ray and extreme ultraviolet emission from comets. In “Comet II” (M. C. Festou, H. U. Keller, and H. A. Weaver, eds.), pp. 631–643. Univ. Arizona Press, Tucson.